Bull Earthquake Eng (2011) 9:893–930
DOI 10.1007/s10518-011-9255-5

ORIGINAL RESEARCH PAPER

Quantification of ground-motion parameters and response spectra in the near-fault region

R. Rupakhety · S. U. Sigurdsson · A. S. Papageorgiou · R. Sigbjörnsson

Received: 25 July 2010 / Accepted: 24 February 2011 / Published online: 18 March 2011

Abstract This study focuses on the characteristics of near-fault ground motions in the forward-direction and structural response associated with them. These ground motions are narrow-banded in nature and are characterized by a predominant period at which structures excited by them are severely affected. In this work, predominant period is defined as the undamped natural period of a single-degree-of-freedom (SDOF) oscillator at which its 5% damped linear elastic pseudo-spectral velocity (*PSV*) contains a clear and dominant peak. It is found that a linear relationship exists between predominant period and seismic moment. An empirical equation describing this relationship is presented by using a large set of accelerograms. Attenuation equations are developed to estimate peak ground velocity (*PGV*) as a function of earthquake magnitude and source-to-site distance. In addition, a predictive equation for spectral shapes of *PSV* (i.e., *PSV* normalized by *PGV*) is presented as a continuous function of the undamped natural period of SDOF oscillators. The model is independent of *PGV*, and can be used in conjunction with any available *PGV* attenuation relation applicable to near-fault ground motion exhibiting forward-directivity effects. Furthermore, viscous damping of the SDOF is included in the model as a continuous parameter, eliminating the use of so-called damping correction factors. Finally, simple equations relating force reduction factors and displacement ductility of elasto-plastic SDOF systems are presented.

Keywords Near-fault ground motion · Forward-directivity · Elastic response spectra · Peak ground velocity · Iso-ductility spectrum · Force reduction factor

R. Rupakhety · S. U. Sigurdsson · R. Sigbjörnsson
Earthquake Engineering Research Center, University of Iceland, Austurvegur 2A, 800 Selfoss, Iceland

A. S. Papageorgiou
Department of Civil Engineering, University of Patras, 26500 Patras, Greece

R. Sigbjörnsson (✉)
Department of Structural Engineering, Norwegian University of Science and Technology, 7491 Trondheim, Norway
e-mail: Ragnar.Sigbjornsson@hi.is

1 Introduction

Near-fault ground motions are known to be a potential cause of severe damage to engineering structures. They usually carry a strong long-period pulse in their velocity records. Directivity effects (see Somerville et al. 1997) and permanent displacement effects (see Abrahamson 2000) have been identified as the most common features of near-fault ground motions. This study is focused on forward-directivity effects in the near-fault region and characterization of elastic as well as inelastic response of single-degree-of-freedom (SDOF) systems.

After the devastating effects of the 1994 Northridge, California, earthquake, simulation of near-fault ground motions and their use in studying structural response gained widespread attention. A primary motivation was the observation that dominant pulses in the velocity records of near-fault ground motion resembled simple waveforms which could be represented by analytical expressions. Many engineers and researchers have used simple waveforms to represent typical velocity pulses observed in near-fault regions. Commonly used waveforms range from simple triangular pulses, square waves, and sinusoidal waves to wavelets of different types. Models proposed by Anderson et al. (1999), Heaton et al. (1995), Makris (1997), Alavi and Krawinkler (2000, 2004), Mavroeidis and Papageorgiou (2003), and Baker (2007) are some examples.

The most important parameters of these models are related to the amplitude and frequency of the velocity pulse. The amplitude of the pulse is representative of the peak ground velocity. Different authors have defined the pulse period in different ways. Nevertheless, they have all found that the pulse period is linearly related to the seismic moment. It has also been found that the pulse period is closely related to the SDOF period where *PSV* attains its maximum value. If the pulse were a simple harmonic with infinite duration, the peak of *PSV* would occur exactly at the pulse period. However, near-fault velocity pulses are of finite duration, defined by the pulse period and the number of half-cycles. Because of this, the period at which *PSV* is the maximum is a fraction of the pulse period, where the fraction depends on the number of half-cycles of the pulse. Apart from this, the presence of other components of ground motion not associated with the pulse itself can also cause the *PSV* to peak at a period different than the pulse period.

The objective of the present paper is to throw light on some of the characteristics of near-fault ground motions and structural response associated with them. We emphasize that the most important characteristics of forward-directivity motion in near-fault areas are peak ground velocity and frequency content. In most models of velocity pulses mentioned above, frequency content is represented by pulse period. However, we quantify the predominant frequency by the period where the *PSV* of a 5% damped linear-elastic oscillator contains a clear and dominant peak. We present robust empirical equations to estimate *PGV* and predominant period from earthquake size, source-to-site distance and other relevant parameters. We then discuss salient features of elastic response spectra of SDOF systems subjected to near-fault ground motions. We present analytical equations of *PGV*-normalized *PSV* (termed here as spectral shapes) as a continuous function of the SDOF period and its level of viscous damping. Finally, characteristics of inelastic response are studied, and equations relating strength reduction factors to displacement ductility of elasto-plastic SDOF systems are presented.

2 Near-fault strong-motion data

Strong-motion data used in this study consist of acceleration records obtained from 29 different earthquakes. In total 93 records are analyzed, the details of which are presented in Table 8 in Appendix 2.

2.1 Data source

The data listed in Table 8 are collected from different sources. Most of the accelerograms are obtained from the NGA database (see Power et al. 2006), along with their associated metadata. Strong-motion records of the 17 and 21 June 2000 earthquakes and the 29 May 2008 Ölfus earthquake in South Iceland were obtained from the ISESD (Internet Site for European Strong-Motion Data) website (Ambraseys et al. 2004). The waveform for WID 90 (EERC basement, see Table 8) was obtained from the database of Earthquake Engineering Research Center, University of Iceland. Metadata related to the records of Icelandic earthquakes were calculated based on several publications, including Sigbjörnsson and Ólafsson (2004), Halldórsson et al. (2007), and Sigbjörnsson et al. (2009). Accelerograms of the 2004 Parkfield earthquake were obtained from CISN (California Integrated Seismic Network) database. In calculating the metadata for records from this earthquake, various publications were considered, including Shakal et al. (2005), Langbein et al. (2005), Liu et al. (2006), Dreger et al. (2005), and Kim and Dreger (2008). Accelerograms at AQK station during the 2009 L'Aquila earthquake were obtained from the online database of the Italian accelerometric network (Luzi et al. 2008). Since we are primarily concerned with forward-directivity effects in this study, permanent displacements (if any) in the ground motion records were removed by subtracting a half-sine pulse from the acceleration records, which was scaled to match permanent displacements computed by a procedure described in Rupakhety et al. (2010).

2.2 Description of metadata

Various parameters of strong-motion records listed in Appendix Table 8 were collected/computed from different sources. Each record is uniquely identified by its waveform identification number (WID. Records generated by the same earthquake share a common earthquake identification number (EID). The location of an earthquake, the date when it occurred, and the station recording the waveform are also listed. Station names reported in Mavroeidis and Papageorgiou (2003) are indicated by abbreviation only, whereas other station names are shown in full. Faulting mechanism, earthquake magnitude (only moment magnitude used in this work), and the component of ground motion being considered are reported along with the peak ground velocity. Different distance metrics are reported, including epicentral distance $\left(r_{epi}\right)$, and Joyner and Boore distance. Hypocentral depth is also reported when available. The length of fault between station and hypocenter (s) and the width of fault between station and hypocenter (d) are also presented. In addition, isochrone velocity ratio as defined by Spudich et al. (2004) is listed for records where it could be computed. Average shear wave velocity in the upper 30 m of the crust $\left(v_{s,30}\right)$ is also provided. Velocity profiles at the stations recording Icelandic earthquakes are not available, and $v_{s,30}$ for these stations are based on their Eurocode 8 (CEN 2004) classification. Parameters that could not be reliably estimated are indicated as 'NA'. Figure 1 shows the distribution of data with respect to magnitude, distance, and faulting mechanism. The distance measure is selected as r_{JB} where available. In case this measure is not available, r_{epi} is used. Stations within 30 km from the source are considered.

3 Relationship between predominant period and seismic moment

Predominant period (T_d) in this work is defined as the period where 5% damped linear-elastic *PSV* reaches its peak value. If more than one peaks of comparable amplitude exist, then the

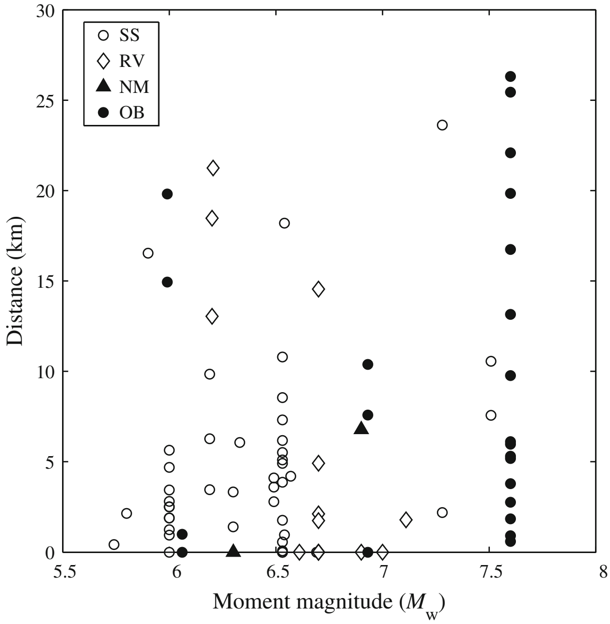

Fig. 1 Distribution of data with respect to magnitude, distance, and the faulting mechanism

longest period is considered. The period of the velocity pulse is related to T_d. On average, the pulse period is about 84% of T_d (Bray and Rodriguez-Marek 2004). An advantage of using T_d is that, unlike pulse periods used in many simple pulse models, it can be unambiguously estimated. Since pulse period has been found to scale linearly with seismic moment, similar scaling for T_d is expected. The relationship between T_d and M_w is modelled by

$$\log(T_d) = \alpha M_w + \beta + \varepsilon \tag{1}$$

where α, and β are model coefficients determined by regression analysis; and ε is a Gaussian-distributed random variable with zero mean and standard deviation σ. The model of Eq. 1 was calibrated by using least squares regression. Records corresponding to sites having $v_{s,30}$ less than 240 m/s are not considered in regression analysis. The predominant periods related to directivity pulses are generally greater than 0.5s. In order that the soil response does not distort the characteristics of directivity pulses, we require the vibration period of the soil to be less than 0.5s. Using the quarter wavelength principle, and considering the upper 30m of the crust, the corresponding shear wave velocity is 240 m/s. The record from COG station of the 1991 Sierra Madre earthquake is of low quality, and could not be processed with confidence. Therefore, this record is not considered in regression analysis. Furthermore, the record from Parachute test site of the 1981 Westmorland earthquake, and the record from Petrolia station of the 1992 Cape Mendocino earthquake contain multiple peaks in their response spectra, making it difficult to identify T_d with confidence. These records are not considered in regression analysis. The regression parameters were found to be $\alpha = 0.47$, $\beta = -2.87$, and $\sigma = 0.18$. Applying the maximum likelihood regression of Joyner and Boore (1993), we did not observe significant difference in the regression parameters for this dataset.

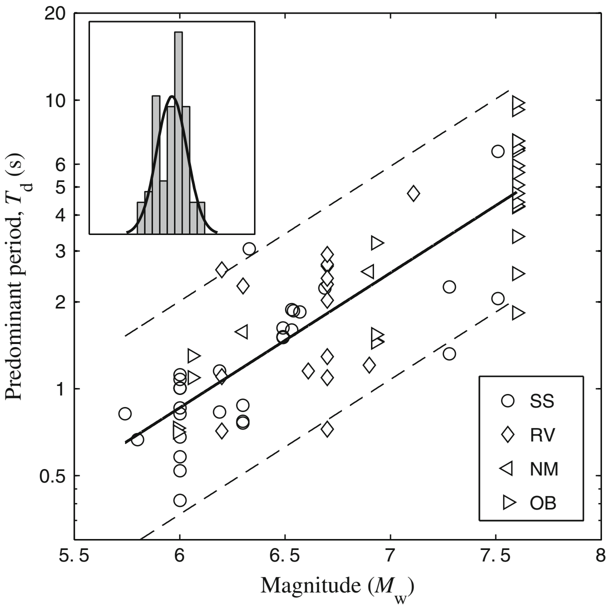

Fig. 2 Scaling of T_d with M_w. The Solid line is the mean value of a least squares line fitted to the data, while the dashed lines correspond to mean$\pm 2\sigma$

The regression line and data points are presented in Fig. 2. The mean value predicted by regression is shown with the solid line, while dashed lines correspond to mean $\pm$ 2σ levels. The distribution of ε is compared with a standard normal distribution in the small inset in the top-left corner of Fig. 2. Somerville et al. (1999) argue that self-similar scaling relationships constrain fault parameters. Such scaling implies that the period of predominant velocity pulse is two times the rise time of slip on the fault. This requires that the coefficient α be equal to 0.5. The coefficient obtained by us is 0.47, which is fairly close to 0.5, and indicates that if self-similar scaling is invoked, the definition of predominant period used by us can be considered as an efficient and unambiguous measure of the pulse period.

4 Attenuation equation for PGV

Empirical relations describing *PGV* as a function of earthquake magnitude, source-to-site distance and other parameters, such as faulting mechanism and site conditions, are abundant in the literature (see Bommer and Alarcon 2006). However, few relations have been developed especially for near-fault conditions with forward rupture-directivity effects. One of the first attempts was made by Somerville (1998), called S98 hereafter, who assumed that *PGV* varies with the square root of the closest distance to fault for stations located at least 3 km away from the fault. Bray and Rodriguez-Marek (2004), called B&R-M04 hereafter, emphasized the need to predict *PGV* at distances closer to the fault than 3 km as well, and used a simple functional form to perform regression analysis of *PGV* data against earthquake magnitude and the closest distance to rupture.

4.1 Attenuation model

The basic functional form adopted in this study is similar to the one used by B&R-M04 and is mathematically expressed as

$$\log\left(PGV_{ij}\right) = a + bM_w + c\log\left(R^2 + d^2\right) + \eta_i + \varepsilon_{ij} \tag{2}$$

where PGV_{ij} is the *PGV* of the jth recording from the ith event; M_w is the moment magnitude of event i; R is the distance (measured in km) of the jth recording obtained from the ith event; a, b, c, and d are regression parameters; and η_i and ε_{ij} represent inter- and intra-event variations. The error terms η_i and ε_{ij} are assumed to be independent, normally-distributed random variables with variances σ_1^2 and σ_2^2, respectively. The total standard deviation associated with estimated *PGV* can be computed from the following equation.

$$\sigma_t = \sqrt{\sigma_1^2 + \sigma_2^2} \tag{3}$$

For distance measure R, we use r_{JB} when rupture model is available and r_{epi} otherwise. Furthermore, we select only those stations within 30 km from the source. The data from COG station of the 1991 Sierra Madre earthquake is excluded in regression due to the reasons explained in Sect. 3 above. In addition, data obtained at sites with $v_{s,30}$ less than 240 m/s are excluded. This implies that the results obtained are applicable to those sites where significant soil effects are not expected. The decision to exclude soft soil data from regression was made because we found that the data was not sufficient to reliably constrain the soil effects by using site coefficients (or $v_{s,30}$) in the regression model. We use base 10 logarithms throughout this work. The model of Eq. 2 was calibrated by using the maximum likelihood method of Joyner and Boore (1993). Regression constants and associated values of standard deviations are shown in Table 1. It was found that the magnitude coefficient b is very small, indicating that *PGV* is almost magnitude-independent in the near-fault region. Magnitude scaling obtained by us is much weaker than that obtained by S98 and Alavi and Krawinkler (2000), called A&K00 hereafter. B&R-M04 also observed that their magnitude scaling was weaker, and their magnitude scaling parameter, b, in base 10 logarithmic units, is 0.15, which is close to our results.

Figure 3 compares PGV data with the model of Eq. 2 and model parameters of Table 1. For comparing attenuation of *PGV* with distance, we normalize observed *PGV* with a magnitude-scaling term (magnitude-normalized). For comparing scaling of *PGV* with magnitude, we normalize observed *PGV* with distance (distance-corrected). In Fig. 3a, attenuation of magnitude-corrected *PGV* is plotted against model prediction. It is seen that the model captures attenuation of *PGV* with distance reasonably well. Figure 3b shows scaling of distance-corrected *PGV* with magnitude. A quadratic magnitude term was added to the model of Eq. 2. This resulted in decrease of *PGV* at magnitudes larger than 7.0. To avoid this effect, we constrained the model in such a way that the magnitude scaling term becomes a constant at a certain magnitude, which was determined iteratively to ensure continuity. The final model is of the following form.

Table 1 Regression coefficients for the model of Eq. 2

a	b	c	d	σ_1	σ_2	σ_t
0.98	0.13	−0.10	0.66	0.099	0.132	0.17

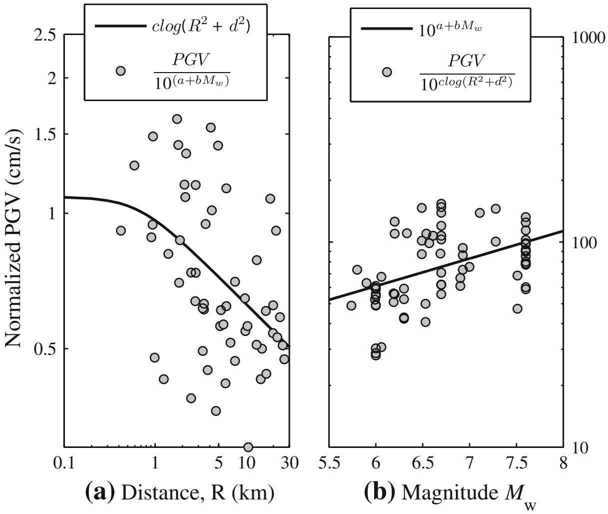

Fig. 3 Comparison of the model of Eq. 2 with the data. (**a**) Attenuation of magnitude-corrected *PGV* with distance. (**b**) Scaling of distance-corrected *PGV* with magnitude

Table 2 Regression coefficients for the model of Eq. 4

a	b	c	d	e	M_{sat}	σ_1	σ_2	σ_t
−5.17	1.98	−0.14	−0.10	0.75	7.0	0.081	0.135	0.16

$$\log\left(PGV_{ij}\right) = \begin{cases} a + bM_w + cM_w^2 + d\log\left(R^2+e^2\right) + \eta_i + \varepsilon_{ij} & \text{if } M_w \le M_{sat} \\ a + bM_{sat} + cM_{sat}^2 + d\log\left(R^2+e^2\right) + \eta_i + \varepsilon_{ij} & \text{otherwise} \end{cases} \quad (4)$$

The results of regression analysis are shown in Table 2, and the comparison of data with the model is shown in Fig. 4. In the legend of Fig. 4, $F\,(M_w)$ is the magnitude term of Eq. 4, which is equal to $a + bM_w + cM_w^2$ for $M_w \le M_{sat}$ and $a + bM_{sat} + cM_{sat}^2$ otherwise. With the modified model, the standard deviation of residuals is slightly reduced. It should be noted that the use of the model for magnitudes below 5.5 is not recommended.

4.2 Directivity predictor

Another important aspect we investigate in this work is the effect of directivity. A parameter to quantify the amount of directivity at a given station for a given event is required. Somerville (2000) proposed the ratio of the length of fault between site and hypocenter and the site azimuth as a measure of directivity. Spudich et al. (2004) showed that the isochrone velocity ratio (i.e., average isochrone velocity normalized by shear wave velocity) behaves similarly to the directivity parameters of Somerville (2000). Isochrone velocity ratio $\tilde{c}$ was computed for most of the stations used in this study. For those records, where reliable information regarding the rupture surface is not available, $\tilde{c}$ cannot be estimated. In a recent study Spudich and Chiou (2008), called S&C08 hereafter, proposed a directivity predictor, based on isochrone velocity ratio and hypocentral radiation pattern. We attempt to apply their idea in our attenuation model of *PGV*. The directivity predictor we use is designated DP (directivity predictor) and is given by

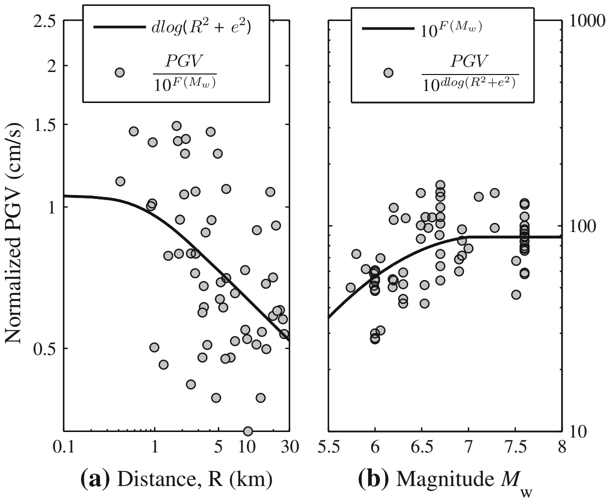

Fig. 4 Comparison of the model of Eq. 4 with data. (**a**) Attenuation of magnitude-corrected *PGV* with distance. (**b**) Scaling of distance-corrected *PGV* with magnitude

$$DP = CS\Re \tag{6}$$

$$C = \frac{\min(\tilde{c}, 2.45) - 0.8}{2.45 - 0.8} \tag{7}$$

$$S = \log[\min(75, \max(s, d))] \tag{8}$$

where s and d are as defined in Sect. 2.2, $\tilde{c}$ is isochrone velocity ratio as defined above, and $\Re$ is scalar radiation pattern amplitude, as defined in S&C08. We use strike-normal or strike-parallel hypocentral radiation pattern with a water level of 0.2 at the nodes, depending upon which component is being considered. For further details on radiation patterns and the reasoning behind Eqs. 6–8, readers are referred to S&C08.

We found that the effect of $\Re$ in the directivity predictor is not significant. At sites very close to the fault, the radiation is dominated by a small area of the fault closest to the station. This might be the reason why the radiation pattern based on the hypocenter is not correlated strongly to *PGV* data being considered here, which come predominantly from stations within a few kilometers from the fault. Therefore, we drop the term $\Re$ in Eq. 6.

Figure 5 shows the correlation between the directivity predictor $DP = CS$ and the residuals of the model presented in Eq. 4. It can be seen that the correlation is very weak. The correlation coefficient was found to be 0.05. The correlation was found to increase to a maximum value of 0.1 when the number '2.45' in Eq. 7 was changed to 1.75. Changing the capping distance, used as 75 km in Eq. 8, did not result in an improved correlation between the directivity predictor and the residuals. Given such weak correlation, we judge that adding the directivity term in the model does not result in an improvement of the model.

These results indicate the limitations of the directivity parameter being considered, however, a general conclusion about their usefulness should not be drawn only based on these results, which are obtained from a limited amount of data. It is also to be noted that the directivity parameter considered here is based on average isochrone velocity. While $\tilde{c}$ could be modified to the actual isochrone velocity closest to station instead of the average isochrone velocity over the rupture area, such an approach is helpful only if the rupture process is well understood. For future predictions, the heterogeneity of slip (amplitude and velocity) over

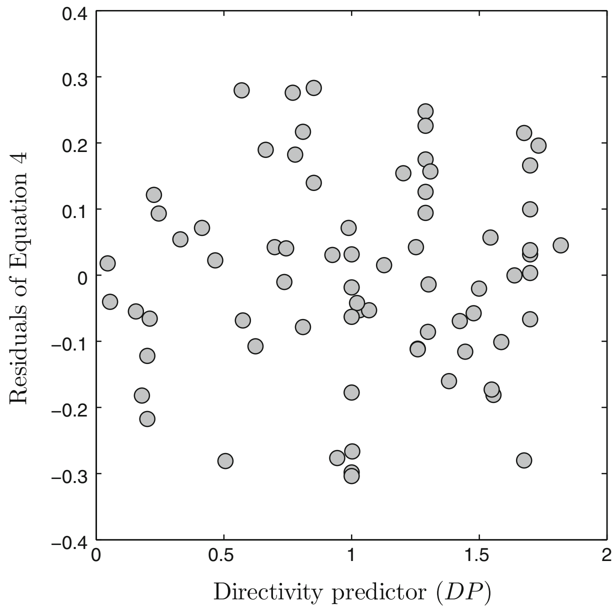

Fig. 5 Residuals of the PGV attenuation model of Eq. 4 display no clear dependence on the directivity parameter based on average isochrone velocity

the rupture area is impossible to predict with the current state of knowledge; thus, using the exact isochrone velocity is of little use.

4.3 Comparison with other attenuation models

In Fig. 6 we compare the model of Eq. 4 and the associated parameters of Table 2 with models proposed by B&R-M04, S98, A&K00, and Halldorsson et al. (2010), hereafter called HM&P10. These authors use the closet distance to rupture as their distance metric. For comparing their model with ours, we assume a vertical strike-slip event. The thick black line in Fig. 6 corresponds to the mean prediction of the proposed model, while upper and lower fractals with 2 standard deviations are shown by black dashed lines. Circles indicate observed values of *PGV*. *PGV* corresponding to all magnitudes are shown, and the model predictions are computed at magnitude 6.6, which is also the mean magnitude of our data. The mean prediction of B&R-M04 is shown with the solid blue line. The dashed red line, the dashed blue line, and the solid red line represent mean predictions of S98, A&K00, and HM&P10, respectively.

We note that the magnitude scaling parameters of A&K00 and S98 are high, and our data do not support such a strong magnitude dependence of *PGV*. On the other hand, magnitude scaling is zero in HM&P10. The attenuation of *PGV* above distances greater than 7 km is very fast in the Model of Bray and Rodriguez-Marek. Fast attenuation in HM&P10's model is related to their functional form. In their model, *PGV* attenuates exponentially with distance. Such exponential attenuation is not supported by our data, as shown in Fig. 6.

5 Elastic response spectra

Earthquake response spectra, first introduced by Biot (1933), are widely used for designing and assessing structures subjected to strong ground motion. Following the works of Housner

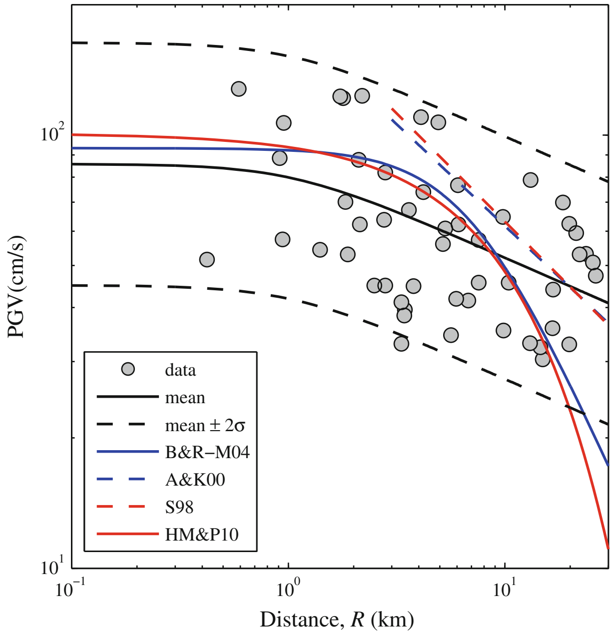

Fig. 6 Comparison of the model of Eq. 4 with observed data (circles) and the models of other authors as indicated in the legend (see text above for legend keys)

(1959) and Newmark et al. (1973), it has become a standard tool to characterize important features of earthquake accelerograms and to evaluate structural response to earthquake-induced ground shaking. Modern design codes for earthquake resistance specify seismic action on structures in terms of design spectra, a statistical representation of response spectra constructed from accelerograms recorded during past earthquakes. Because a majority of accelerograms are recorded far away from causative faults, code-specified design spectra are dominated by response spectra of ground motion in the far-fault region.

Accelerograms from large earthquakes in the recent past have shown that response spectra of near-fault ground motions, mainly of those affected by forward-directivity effects, are different from those of far-fault ones. One of the characteristic differences between the two is the narrow-banded spectral structure of the former. Response spectra of forward-directivity-affected near-fault ground motion exhibit spectral peak values in a narrow band of periods near the predominant period of ground motion. Predominant period increases with increasing earthquake magnitude, as discussed in Sect. 3. Such magnitude scaling has two important implications for elastic response spectra. First, the acceleration response of moderate-to-large earthquakes is stronger than that of large earthquakes in the high-frequency region; the trend being reversed at longer periods. Second, peak spectral accelerations of moderate-to-large earthquakes are larger than those of very large earthquakes (Somerville 2000; Mavroeidis et al. 2004).

The differences in the response of structures to near-fault and far-fault ground motions imply that design spectra, derived from more far-fault accelerograms than near-fault ones, are biased. They are not capable of capturing the impulsive nature of near-fault ground motion and often lead to unreliable estimates of seismic action on engineering structures located near an earthquake fault. Therefore, it is essential to develop design spectra specifically suitable for ground motion in the near-fault area. One of the first systematic efforts was made by Somerville et al. (1997). They proposed broad-band amplification factors for spectral ordinates of ground motion prediction models. The narrow-banded nature of pulse-like ground-motion, however, suggests that a more accurate model would amplify spectral accelerations only in a narrow spectral band close to the predominant period of ground motion. We also note that most ground-motion prediction models are not exclusively based on non-pulse-like ground motion. Their calibration is usually performed by using pulse-like as well as non-pulse-like ground motion. Amplification factors for existing ground motion prediction models would be more meaningful if they were calibrated only from non-pulse-like ground motions. In this study, we develop response spectral model applicable strictly to near-fault ground motion exhibiting forward-directivity effects. The proposed model is based on recorded accelerograms within 30 km from the fault generated by earthquakes ranging in magnitude between 5.5 and 7.6. This model should not be extrapolated in terms of earthquake magnitude or source to site distance.

5.1 Elastic response spectral shapes

In the following, the term 'elastic spectra' is used for under-damped linear elastic pseudo-spectral velocity, *PSV*, and the term 'spectral shape' is used for *PSV* normalized by the peak ground velocity, *PGV*. The predominant period (T_d) is as defined in Sect. 3, and increases with increasing earthquake magnitude. We present an illustration of this scaling effect on spectral shapes in Fig. 7.

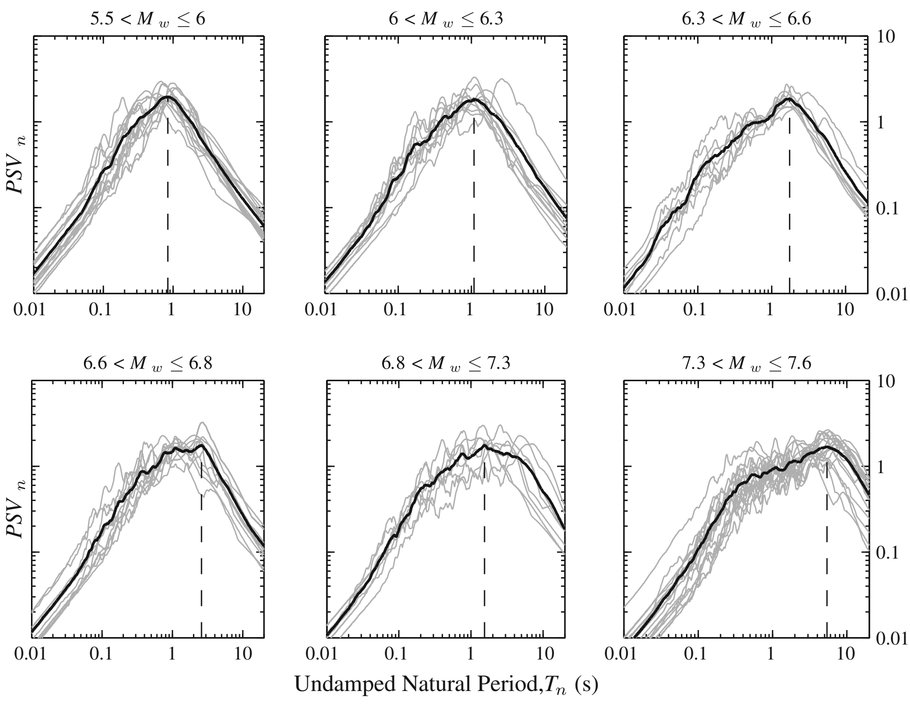

Fig. 7 Spectral shapes of near-fault ground motion grouped into six magnitude bins. The range of magnitude in each bin is shown above the plots. Grey lines are spectral shapes of individual accelerograms, while thick black lines correspond to mean values. The dashed vertical line indicates the peak of mean spectral shape

Table 3 Grouping of near-fault records into different magnitude bins

Bin	M_w range	No. of records
1	$5.5 < M_w \leq 6.0$	14
2	$6.0 < M_w \leq 6.3$	11
3	$6.3 < M_w \leq 6.6$	8
4	$6.6 < M_w \leq 6.8$	12
5	$6.8 < M_w \leq 7.3$	8
6	$7.3 < M_w \leq 7.6$	18

In Fig. 7, 5% damped spectral shapes are presented. Only those records included in $M_w - T_d$ scaling presented in Sect. 3 are considered. To illustrate the effect of magnitude on spectral shapes, ground motions are grouped into six distinct magnitude bins as indicated in the figure. The bins are listed in Table 3 along with bin magnitude ranges and the number of records falling into each bin. An ideal bin should be as narrow as possible to represent the continuous nature of magnitude but near-fault ground motion records are not abundant and bin classification is therefore dictated by lack of data. Due to this limitation, we were forced to use non-uniform magnitude bins as shown in Table 3. One of the characteristic features of spectral shapes presented in Fig. 7 is the narrow velocity-sensitive region. Unlike far-fault spectral shapes, near-fault ones have relatively wider acceleration-sensitive and displacement-sensitive regions but a narrower velocity-sensitive region. This narrow velocity-sensitive region is where the peak of *PSV* generally occurs. The location of peak is shifted to the right (longer periods) as earthquake magnitude increases. As is evident from Fig. 7, peak locations vary from about 0.8 s to about 5.5 s for bins 1 and 6, respectively. Careful examination of the spectral shape of bin 5 indicates an apparent contradiction, with its peak occurring at a smaller natural period than that of bin 4. However, this bin shows a wider velocity-sensitive region ranging from about 1 s to about 3 s with almost-constant ordinates. The reason for this wider velocity-sensitive region is the relatively large size of this bin (wider range of magnitudes), which could not be avoided due to the lack of data. It should be noted that although bins 1 and 5 appear to have the same size as defined in Table 3, their effective size are not the same. Bin 1 contains records from earthquakes having magnitudes 5.74 to 6.0, while Bin 5 contains records from earthquakes having magnitudes 6.8 to 7.28.

The magnitude dependence of spectral shapes observed in Fig. 7 is consistent with the notion that larger earthquakes have a richer energy content in the long-period range. This also implies that, at short periods, response spectra of moderate-to-large earthquakes in the near-fault region are higher than those of large earthquakes. Figure 8 clearly demonstrates this effect. Gray lines in the figure represent the *PSV* of 'individual' records. Solid and dashed lines represent mean *PSV* of the first and the sixth bin, respectively. It is evident that smaller earthquakes have, on average, higher spectral ordinates at short periods than the larger ones, the trend being reversed at longer periods. In addition, peak amplitudes of average spectral shapes of the two bins are comparable. This implies that peak response spectral ordinates of small earthquakes are comparable to those of larger ones but occur at different periods. This is a remarkable feature of the response spectra of near-fault ground motion. These properties of spectral shapes allow them to be modelled by simple continuous functions of T_n and earthquake magnitude. In the following, we develop such a model.

5.2 Equations for elastic response spectra

In most modern applications, ground motion prediction equations (GMPEs) are used to obtain elastic response spectra for design and risk assessment of structures. GMPEs for 5% damped

Fig. 8 *PSV* of small and large earthquakes. Solid and dashed lines represent mean spectral shapes of bin 1 and bin 6, respectively

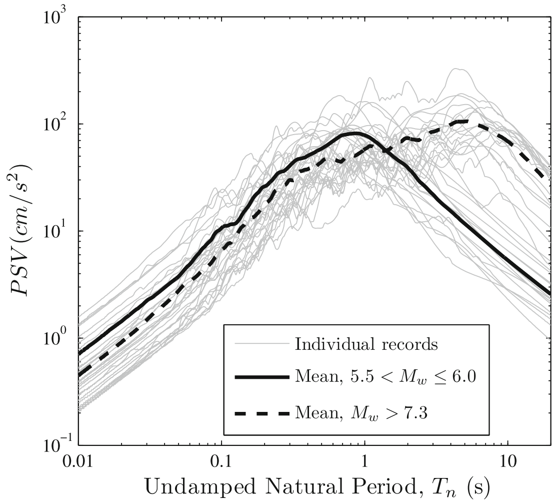

linear elastic *PSA* (pseudo spectral acceleration) at discrete values of T_n are abundant in the literature. Some examples of such equations are Abrahamson and Silva (1997), Boore et al. (1997), Sadigh et al. (1997), Ambraseys et al. (2005), Akkar and Bommer (2007) etc., more recent ones being the Next Generation Attenuation (NGA) equations (see Abrahamson et al. 2008). A comprehensive report on ground-motion prediction equation is given in Douglas (2003). Similar equations for inelastic response are given in Rupakhety and Sigbjörnsson (2009a,b) and Bozorgnia et al. (2010). These conventional GMPEs are associated with a matrix of model coefficients at discrete values of T_n.

A different approach to predicting spectral accelerations has recently been adopted by Graizer and Kalkan (2009). They proposed ground-motion spectral shapes for 5% damped *PSA* normalized by peak ground acceleration (*PGA*). Their spectral shapes are continuous functions of T_n. Such an approach significantly facilitates implementing the model. Another distinct advantage of this approach lies in the option to use spectral shapes in conjunction with any attenuation model of *PGA*, thus allowing the use of various models of attenuation relations to estimate response spectra.

We use a similar approach in developing spectral shapes for pulse-like ground motion. It is assumed that spectral shapes depend on variables such as earthquake magnitude, source-to-site distance, shear wave velocity at recording sites, basin effects, etc. For a description of different factors controlling spectral shapes, readers are referred to Graizer and Kalkan (2009). We assume that spectral shapes are predominantly influenced by magnitude of an earthquake and do not consider distance dependence in the near-fault zone. Whereas Graizer and Kalkan (2009) used *PGA*-normalized *PSA* as their spectral shapes, we consider *PSV* normalized by *PGV*. This does not limit the applicability of the model developed herein because *PSV* and *PSA* are related through T_n. Once spectral shapes are available, they can be scaled with *PGV* to obtain *PSV*, which is easily converted to *PSA*. The attenuation relation of *PGV* for ground motion records considered here has already been presented in Sect. 4.

5.3 Model function for spectral shapes

We use an empirical approach similar to that of Graizer and Kalkan (2009) in finding a suitable function for spectral shape. The suggested model is defined by a sum of two functions -$F_1(T_n, M_w)$ and $F_2(T_n, M_w)$. Both of these functions are continuous with respect to the oscillator period (T_n) for a given magnitude (M_w). The first function is a modified 'log-normal type' function and is mathematically expressed as

$$F_1(T_n, M_w) = I_1(M_w)\exp\left[-0.5\left\{\frac{\ln(T_n) + C(M_w)}{W(M_w)}\right\}^2\right]T_n \tag{9}$$

where $I_1(M_w)$ controls the amplitude of this bell-shaped function, while its location and scale are governed by $C(M_w)$ and $W(M_w)$, respectively. The second function, which is a modified form of SDOF transfer function, is expressed by the following mathematical equation

$$F_2(T_n, M_w) = I_2(M_w)\left[\left\{1 - \left(\frac{T_n}{T_m}\right)^{\theta}\right\}^2 + 4D_m^2\left(\frac{T_n}{T_m}\right)^{\theta}\right]^{-0.5} T_n \tag{10}$$

where $I_2(M_w)$ controls the overall amplitude of this function. This function is linearly increasing at short periods and exhibits a bump peaking close to T_m-the amount of bump is controlled by D_m. The rate of decay of F_2 at long periods is controlled by θ. Both D_m and θ depend on M_w. With magnitude dependence implied by binning, we drop M_w from our equations with the understanding that the parameters are calibrated independently for each magnitude bin. By summing $F_1(T_n)$ and $F_2(T_n)$, spectral shape for normalized PSV, denoted by PSV_n, is given by the following equation.

$$PSV_n = \left[I_1\exp\left\{-0.5\left(\frac{\ln(T_n) + C}{W}\right)^2\right\} + I_2\left\{\left(1 - \left(\frac{T_n}{T_m}\right)^{\theta}\right)^2 + 4D_m^2\left(\frac{T_n}{T_m}\right)^{\theta}\right\}^{-0.5}\right]T_n \tag{11}$$

5.4 Calibration of spectral shapes

The model spectrum, Eq. 11, is calibrated against the mean spectral shapes of different magnitude bins. Non-linear optimization, and verification by visual inspection, is used in estimating the parameters.

5.4.1 Model parameters

At the first step, the parameter θ is constrained. This parameter controls the slope of the spectrum at long periods. At long periods, the response spectra computed from ground motion records is not reliable due to the effects of low-pass filtering that is commonly employed in data processing. In this work we constrain the slope of the long period spectra (i.e. θ in our model) by the asymptotic behaviour of the Fourier near-fault source spectrum (see, for instance, Brune 1970) using the random vibration theory. The procedure is outlined in more detail in Appendix 1. Following this approach, θ was constrained to a value of 2.0. Note that the reliable period (dictated by the quality of data) up to which the proposed spectral shapes can be used depends on the earthquake magnitude. As a general recommendation, the spectral shapes proposed here can be used for SDOF periods less than about 2 times the predominant period. Nevertheless, we present the results for periods up to 10 seconds for all magnitude

Table 4 Parameters of Eq. 11 for different magnitude bins

Bin	I_1	T_m	D_m	I_2
1	1.43	0.85	0.50	1.51
2	1.07	1.15	0.55	1.35
3	0.95	1.55	0.62	1.27
4	0.88	1.80	0.65	1.10
5	1.35	2.45	0.67	0.94
6	0.95	4,95	0.79	0.54

bins, and emphasize that the long period part of the spectrum is approximated by the procedure outlined in Appendix 1. While we recognize the possible errors in estimating response spectral ordinates at such long periods, we believe that these errors are not critical in terms of engineering application of the proposed model. One might argue that the long-period spectral ordinates are critical for very tall and flexible structures as they have long fundamental period of vibration. But, given the very small amplitudes of spectral ordinates at these periods, the total response of such structures is most likely controlled by higher modes of vibration, more so if inter-story drift demands are considered as the response quantity of interest.

The results obtained by calibrating the remaining parameters showed that W and C can be taken as constant quantities equal to 1 and 1.4, respectively. The other parameters are shown in Table 4. The quality of the fit between simulated shapes (i.e., spectral shapes approximated by Eq. 11) and mean spectral shapes of actual ground motion is presented in Fig. 9. Simulated shapes are represented in Fig. 9 by thin dark lines. Mean spectral shapes, on the

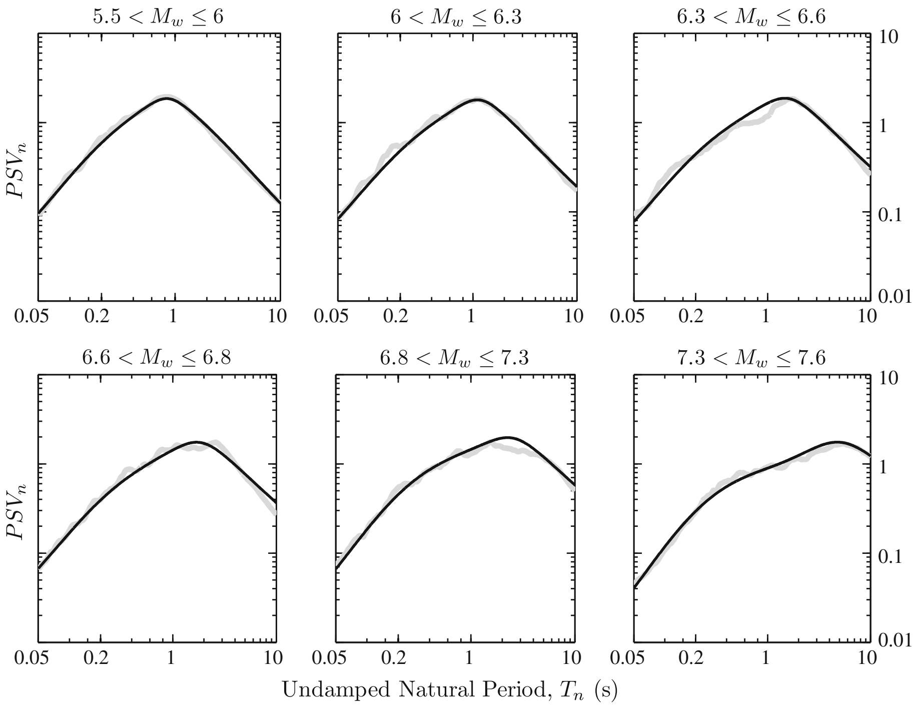

Fig. 9 Comparison of simulated spectral shapes with mean spectral shapes

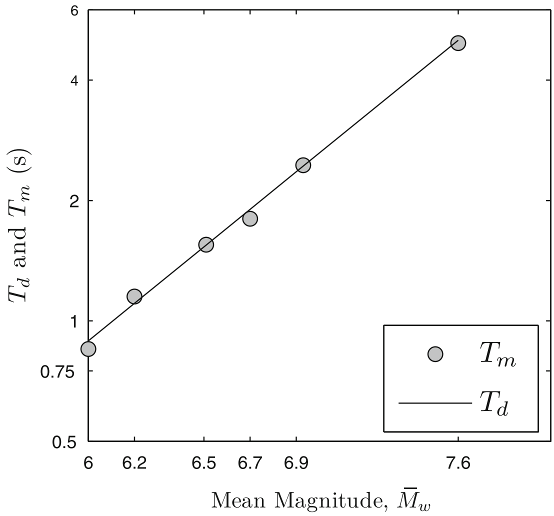

Fig. 10 Relationship between T_m and mean bin magnitude

other hand, are plotted as thick gray lines. It is observed that simulated spectral shapes match mean spectral shapes very well.

5.4.2 Magnitude dependence of model parameters

Careful examination of Table 4 shows that some of the parameters listed are strongly correlated with the average magnitude of their corresponding bins. The model being proposed could possibly be simplified by expressing some of these parameters in terms of M_w. As an average measure of M_w, we select the mean value in a bin and explore its relation with different parameters listed in Table 4.

We found a strong relation between T_m and mean magnitude. The mean magnitudes for the bins selected in this study are 6, 6.2, 6.5, 6.7, 6.9 and 7.6, respectively, for bins 1, 2, 3, 4, 5 and 6. Their relation with T_m is shown in Fig. 10. Note that the vertical axis is in logarithmic scale. Grey circles in the figure represent the values of T_m from Table 4 plotted against the mean bin magnitude. The relation between T_m and median magnitude was found to be very similar to the relation between predominant period and magnitude (see Eq. 1). For comparison, this equation is shown with the black line in Fig. 10. This is expected following the definition of the predominant period. The figure clearly shows that T_m can be taken as equal to T_d whose mean value is estimated from Eq. 1. These observations allow us to simplify the spectral shape model with the following equation.

$$PSV_n = \left[I_1 \exp\left\{-0.5\left(\ln\left(T_n\right)+1.4\right)^2\right\} + I_2 \left\{\left(1-\left(\frac{T_n}{T_d}\right)^2\right)^2 + 4D_m^2\left(\frac{T_n}{T_d}\right)^2\right\}^{-0.5}\right] T_n \tag{12}$$

We emphasize that there are only three free parameters in Eq. 12 and all others have been constrained. We recalibrated the remaining parameters and found a strong relationship between mean bin magnitude and I_2, which is displayed in Fig. 11. Their relationship can be described by the straight line plotted in Fig. 11. The equation of the fitted line is also presented

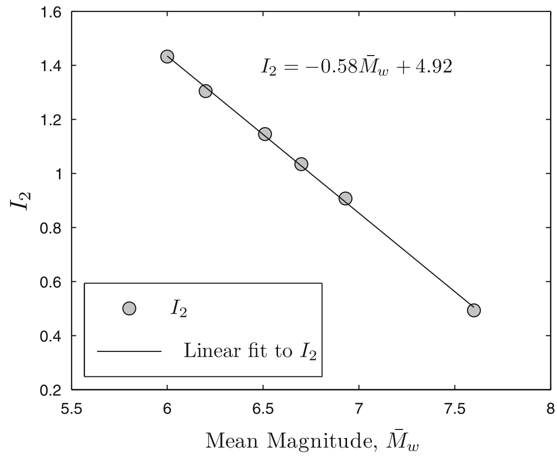

Fig. 11 Relationship between I_2 and mean bin magnitude

Table 5 Parameters of Eq. 13 for different magnitude bins

Bin	I_1	D_m
1	1.43	0.46
2	1.07	0.52
3	0.95	0.58
4	0.88	0.65
5	1.27	0.79
6	1.11	0.77

in the figure. With these additional constraints applied to I_2, the approximate spectral shape is given by:

$$PSV_n = \left[I_1 \exp\left\{-0.5\left(\ln\left(T_n\right)+1.4\right)^2\right\} + \left(4.92 - 0.58M_w\right)\left\{\left(1-\left(\frac{T_n}{T_d}\right)^2\right)^2 + 4D_m^2\left(\frac{T_n}{T_d}\right)^2\right\}^{-0.5}\right] T_n \tag{13}$$

The free parameters of Eq. 13 were recalibrated, and their values are presented in Table 5. Finally, the comparison of approximate spectral shapes computed by using Eq. 13 with its parameters from Table 5 and mean spectral shapes is displayed in Fig. 12. These results indicate that the proposed model can capture the salient features of spectral shapes of forward-directivity-affected near-fault ground motion as a continuous function of T_n. The proposed model is simple and involves only two free (independent) parameters. It also considerably facilitates constructing the spectral shapes due to the continuous nature of the function with respect to T_n. We recognize that spectral shapes, to some degree, are affected by source-to-site distance, local soil conditions, and basin-generated effects. Whereas these additional parameters might be useful in applying more robust constraints on spectral shapes, the instances of recorded ground motion with forward-rupture directivity in the near-fault region are not sufficient to model these effects.

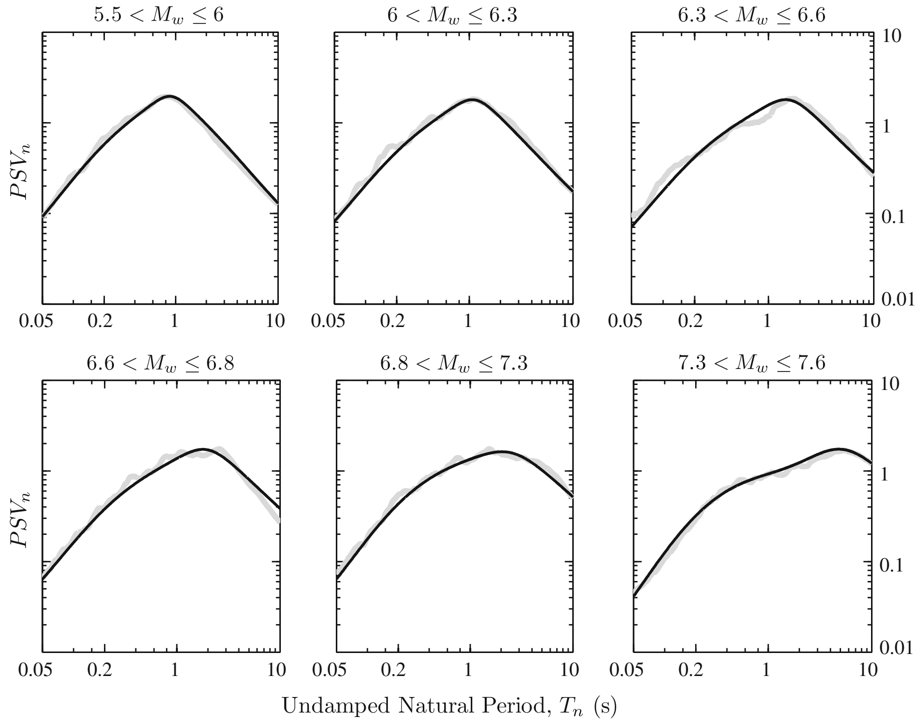

Fig. 12 Comparison of mean spectral shapes of different bins with the approximate spectral shapes computed from Eq. 13 and Table 5

6 Incorporation of viscous damping

The results presented in Sect. 5 correspond to SDOF systems with a viscous damping ratio equal to 5% of critical damping. The conventional approach for creating response spectra for other values of damping has been to modify 5% damped spectra with the so-called damping correction factors (see, for example, Lin and Chang 2003, and references therein). Although such an approach is popular and easy to apply, we believe they involve certain uncertainties. Because highly-damped spectra are smoother than those corresponding to low damping values, the variation of individual spectra from the mean of an ensemble of ground motion decreases as damping level is increased. The approach of modifying 5% damped spectra, on the other hand, not only propagates the uncertainty involved with 5% damped spectra but also introduces additional uncertainty due to simplified damping reduction factors. We present an alternative approach to create response spectral shapes for different levels of viscous damping by evaluating the parameters of the spectral shape model as a function of viscous damping ratio. To accomplish the task, we computed spectral shapes for different values of critical damping ratio (ζ), namely 2%, 5%, 7%, 8%, 10%, 12%, 14%, 17%, and 20%. For damping ratios above 20%, pseudo-spectral velocity tends to differ from spectral velocity, and we therefore limit our analysis to 20% of critical damping.

Initial results indicated that W, C, and T_m are not dependent on the level of damping. It was also found that I_2 is not strongly affected by damping level and can be computed from

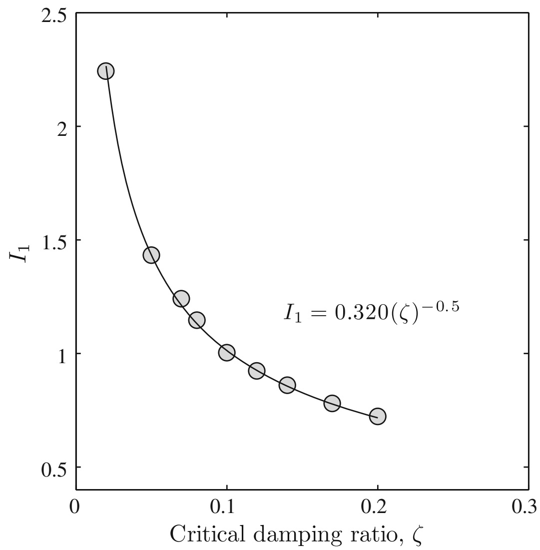

Fig. 13 Relationship between I_1 and viscous damping ratio for the first magnitude bin

the equation shown in Fig. 11. The remaining parameter I_1 displayed strong relationship with damping level. In Fig. 13, their relationship is displayed for magnitude bin 1. Results for other bins are similar, and are not shown. It is observed that I_1 and ζ are related by an equation of the form $I_1 = a\zeta^{-0.5}$, where a is evaluated separately for each bin by fitting a least squares regression line, as shown in Fig. 13 for the first bin. In the proposed model, I_1 contributes to the amplitude of spectral shapes mostly at intermediate frequencies. The power law type of scaling observed for I_1 is similar to the $\sqrt{1/\zeta}$ type of relationship commonly used as damping correction factors.

With the value of I_1 constrained as discussed above, the remaining parameters D_m and was recalibrated. It was observed that D_m increases as the damping level increases. In the proposed model D_m controls the peak of the spectral shape (lower D_m results in higher peak) around a narrow band close to the period where PSV_n is the maximum. It is well known that the effect of damping is to decrease the amplitude of spectral ordinates near the resonant period. In this sense, the observed relation between D_m and ζ is expected. It was found that a liner relationship of the form $D_m = c + d\zeta$ can be used to capture the dependence of D_m on ζ. The relation between D_m and ζ, along with least squares lines and their equations, are shown in Fig. 14 for all magnitude bins These developments make it possible to estimate the spectral shapes for different levels of damping from 2% to 20% and for different magnitudes by using Eq. 13 and its parameters listed in Table 6. The critical damping ratio should be expressed as a fraction in using Table 6 (for example, use $\zeta = 0.02$ if viscous damping ratio is 2% of the critical level).

Finally, we present the comparison between the mean spectral shapes of the different magnitude bins against the simulated shapes using Eq. 13 and its parameters from Table 6 for critical damping ratios of 2% and 20% in Figs. 15 and 16, respectively. The result for 5% of critical damping remains the same as in Fig. 12.

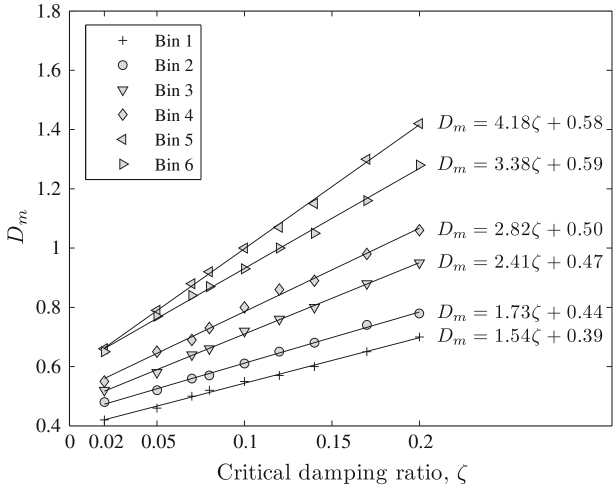

Fig. 14 Relationship between D_m and viscous damping ratio

Table 6 Parameters of Eq. 13 for different magnitude bins and damping ratios

Bin	I_1	D_m
1	$0.320\zeta^{-0.5}$	$1.54\zeta + 0.39$
2	$0.239\zeta^{-0.5}$	$1.73\zeta + 0.44$
3	$0.211\zeta^{-0.5}$	$2.41\zeta + 0.47$
4	$0.204\zeta^{-0.5}$	$2.82\zeta + 0.50$
5	$0.283\zeta^{-0.5}$	$4.18\zeta + 0.58$
6	$0.242\zeta^{-0.5}$	$3.38\zeta + 0.59$

7 Handling uncertainties in spectral shapes

For probabilistic applications, it is beneficial to have a measure of uncertainty in estimated ground motion parameters. Most attenuation relations come with an estimate of standard deviation of residuals from regression analysis. To estimate the uncertainty in *PSV*, it is necessary to have an estimate of standard deviation of PSV_n residuals. In this section we provide such a measure. The residuals in this context are the deviations of response spectral shapes of individual records from the value computed by Eq. 13. We use magnitude of individual records in Eq. 13 to compute spectral shapes and their residuals. Note that the two parameters I_1 and D_m could not be expressed as a continuous function of M_w, and are known for mean bin magnitudes only. In computing the spectral shapes for individual records, we use these parameters corresponding to the mean magnitude of the bin these records lie in. This introduces some approximation which could be minimized if more data are available to construct small magnitude bins. Residuals are computed and specified at base 10 logarithmic scale at different values of T_n. The standard deviation of these residuals is termed $\sigma_{\log PSV_n}$ and is plotted in Fig. 17 as a function of T_n for three different levels of damping. Note that the T_n axis is in logarithmic scale. The figure clearly shows that standard deviation reduces as the damping level increases. This is because as damping ratio increases, spectral shapes become smoother. The decrease in the standard deviation of residuals with increasing damping level

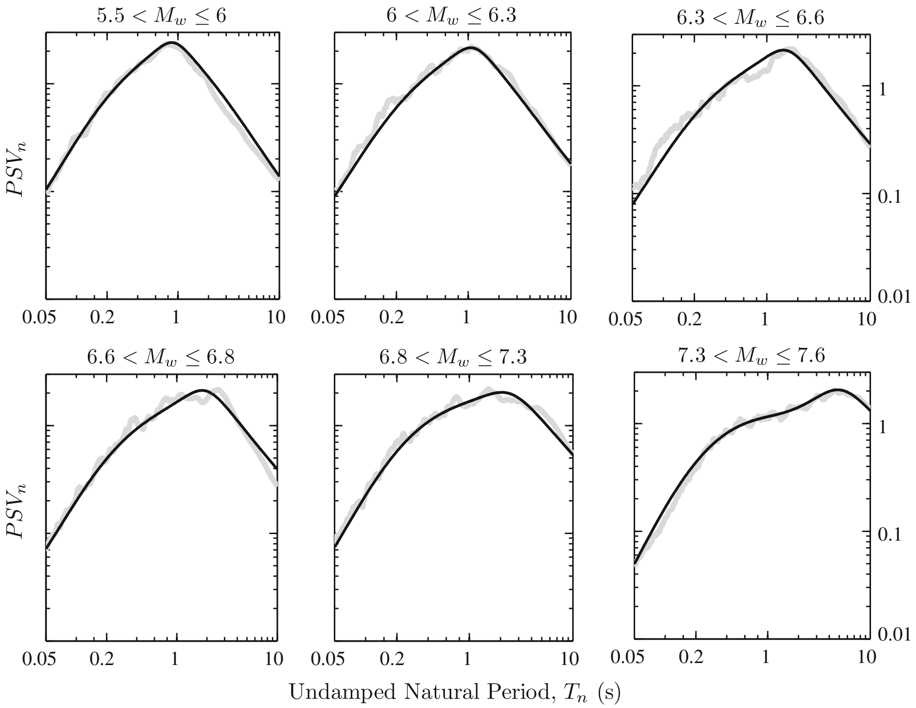

Fig. 15 Comparison of 2% damped mean spectral shapes with the ones simulated by Eq. 13 and Table 6

is the largest in the high-frequency region. We found that uncertainty in spectral shapes predicted by our model is smallest in the range $0.2s < T_n < 4s$. This is, in most cases, the period range of greatest interest for engineering design. We also notice that the variation of $\sigma_{\log PSV_n}$ with T_n can be approximated by a simple curve as represented by the black line in Fig. 18 for 5% damped systems. The equation related to this approximation is the following.

$$\sigma_{\log PSV_n} = \begin{cases} 0.18 - 0.04 \sin\left[2.9\left(\log T_n - 1.7\right)\right] & \text{if } -1.73 < \log T_n < 1.0 \\ 0.16 & \text{if } \log T_n \leq -1.73 \end{cases} \tag{14}$$

We suggest this approximation function, which is similar to the computed values of $\sigma_{\log PSV_n}$, to avoid a long list of $\sigma_{\log PSV_n}$ at discrete T_n values. Equation 14 corresponds to 5%-damped systems. For higher levels of damping, the standard deviations are smaller. On average it was found that standard deviation for damping ratios of 0.02, 0.07, 0.08, 0.1, 0.12, 0.14, 0.17, and 0.2 were 1.06, 0.98, 0.97, 0.95, 0.93, 0.92, 0.90, and 0.88 times that for 5% damped system respectively. In order to compute the standard deviation of PSV from $\sigma_{\log PSV_n}$ and $\sigma_{\log PGV}$, the correlation between PSV_n and PGV need to be established. The computed coefficients of these correlation for our data was found to be negative (−0.2 to −0.3) between SDOF periods of 0.01s and 1s beyond which it increased to 0.3 at a SDOF period of 2s, and then decreased steadily to 0 at about 10s. Because these coefficients are small, PSV_n and PGV can be assumed to be uncorrelated, and the uncertainty in PSV can be approximated from the following equation.

$$\sigma_{\log PSV} = \sqrt{\left(\sigma_{\log PSV_n}\right)^2 + \left(\sigma_{\log PGV}\right)^2} \tag{15}$$

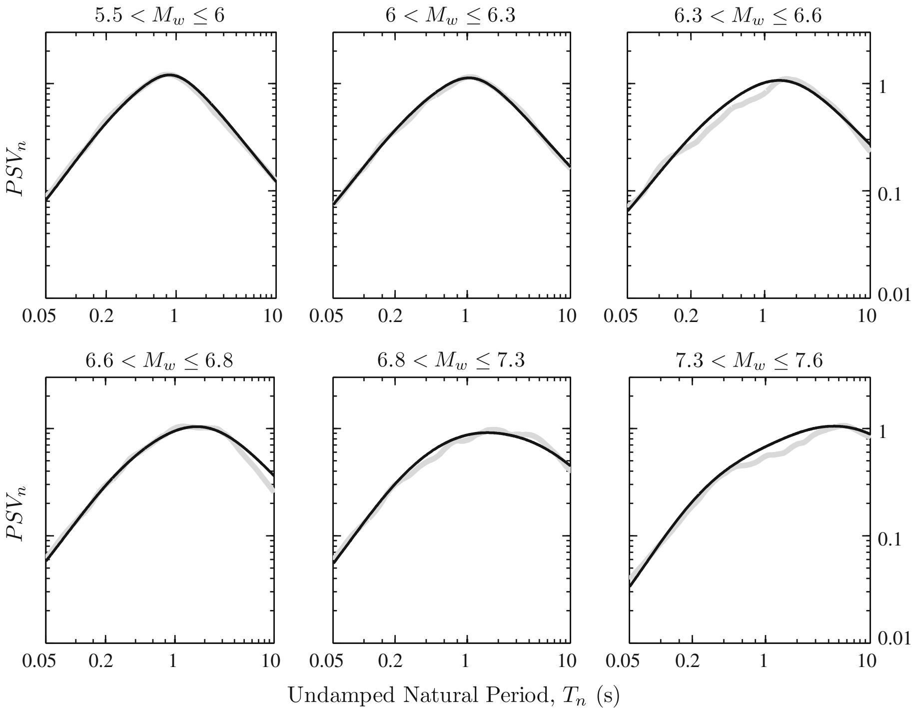

Fig. 16 Comparison of 20% damped mean spectral shapes with the ones simulated by Eq. 13 and Table 6

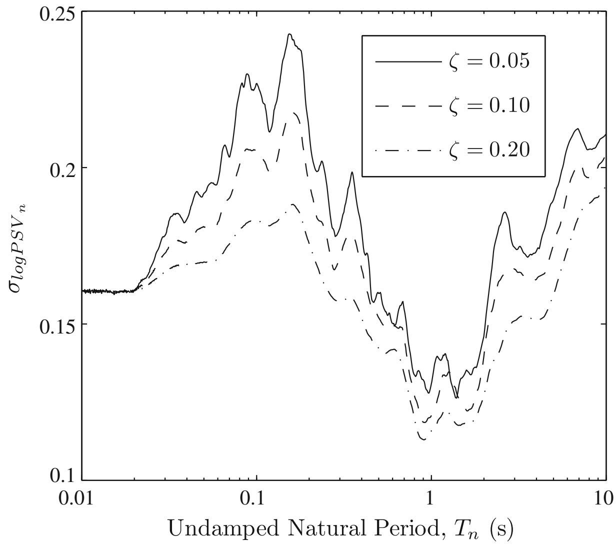

Fig. 17 Standard deviation of residuals of spectral shapes for three different levels of viscous damping

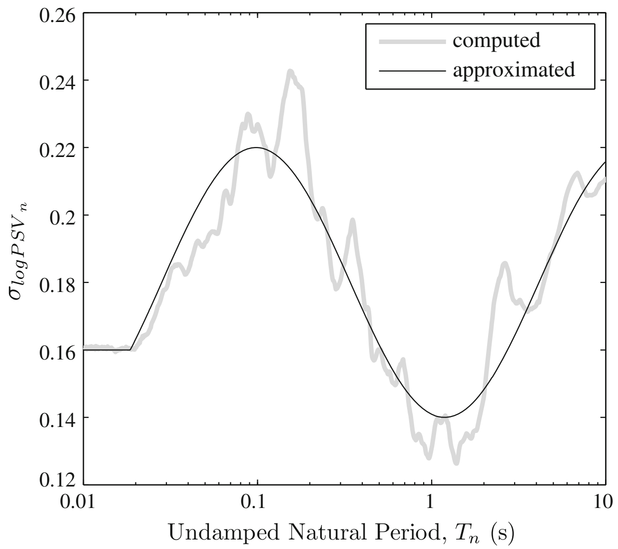

Fig. 18 Standard deviation of residuals for 5% damped spectral shapes as a function of T_n

In Eq. 15, $\sigma_{\log PGV}$ can be computed from any appropriate attenuation equation for PGV, such as the one proposed in Sect. 4.2. The value of $\sigma_{\log PGV}$ computed in Sect. 4.2 was 0.16. Considering this, $\sigma_{\log PSV}$ varies from about 0.21 to 0.27.

In Fig. 19, the distribution of PSV_n residuals is compared with standard normal distribution for nine different values of T_n, as indicated at top of each plot, and for a 5% damped system. The residuals are found to have zero mean in general although there are some differences between the residual distribution and normal distribution. Such differences are commonly experienced and may possibly be due to lack or non-uniform distribution of data. For practical application, an assumption of normal distribution for $\sigma_{\log PSV_n}$, i.e., log-normal distribution for PSV_n seems reasonable from the results presented in Fig. 19.

The model that we have developed here is valid only in the near-fault area (within 20–25 km from the fault) and within the range of earthquake magnitudes considered in this study (5.5 to 7.6 in moment magnitude scale). Furthermore, the model is applicable only if forward-directivity effects are expected. If, in hazard or risk analysis, an analyst uses the proposed model along with other models to account for scenarios not applicable to our model, abrupt changes in scaling of ground motion quantities with respect to distance can result. This leads to the common dilemma of finding a rational way of combining different models. In PSHA, this is modelled as epistemic uncertainty, and the so-called logic trees are applied to combine different ground-motion models. While this approach is, to a large extent, ad-hoc procedure in terms of selecting the weights assigned to different models, a more rigorous approach has not yet evolved. In combining our model with other models valid in the far-field area, we recommend using a weighting function (of distance from the fault) w which the analyst can choose to vary from 1 at the fault plane to 0 at a distance of about 25 km from the fault. Then any far-field model to be combined with the proposed model will be given a weight of 1-w. We recognize that this is an ad-hoc approach, and further research is necessary in finding convincing methods to handle epistemic uncertainties in seismic hazard or risk assessment exercises.

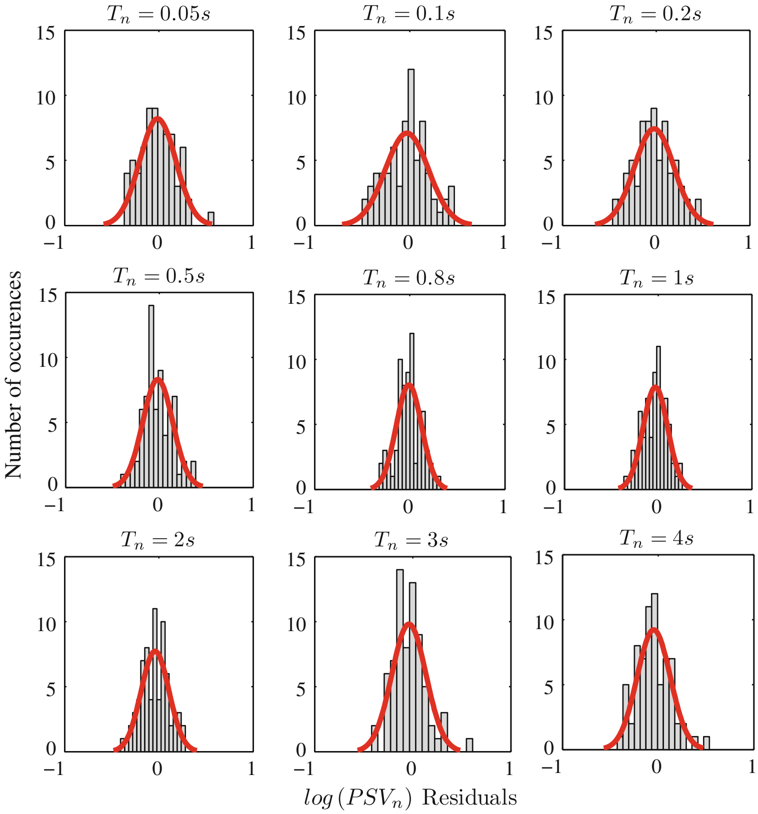

Fig. 19 Distribution of residuals of 5% damped spectral shapes compared with a standard normal distribution

8 Inelastic response and force reduction factor

Force-based design of engineering structures for earthquake resistance generally requires inelastic response spectra of SDOF systems to estimate design lateral strengths. Inelastic response spectra for earthquake ground motion are typically constructed by reducing elastic response spectra by the so-called force reduction factor or structural behaviour factor. Hysteretic energy dissipation during inelastic deformation is a major contributor to these reduction factors apart from damping and structural over-strength. The reduction in design forces due to hysteretic energy dissipation (R_μ) is defined as the ratio of elastic strength demand to inelastic strength demand required to maintain a displacement ductility (μ) less than or equal to a pre-determined target ductility ratio when subjected to the same excitation. Miranda and Bertero (1994) provide detailed review on R_μ and the factors affecting its magnitude. Other researchers carrying out extensive studies on force reduction factors include Borzi and Elnashai (2000); Jalali and Trifunac (2008), and Watanabe and Kawashima (2002), to name a few. The results of past studies have shown that R_μ depends mainly on μ and T_n. In this section we present the relationship between R_μ, μ, and T_n for forward-directivity affected near-fault ground motions.

To explore the dependence of R_μ on SDOF period and target ductility level, yield strength (iso-ductile) spectra were computed for target displacement ductility levels of 1.5, 2, 3, 4, 5, and 6. The hysteretic behaviour of inelastic SDOF was assumed to be elastic-perfectly-plastic,

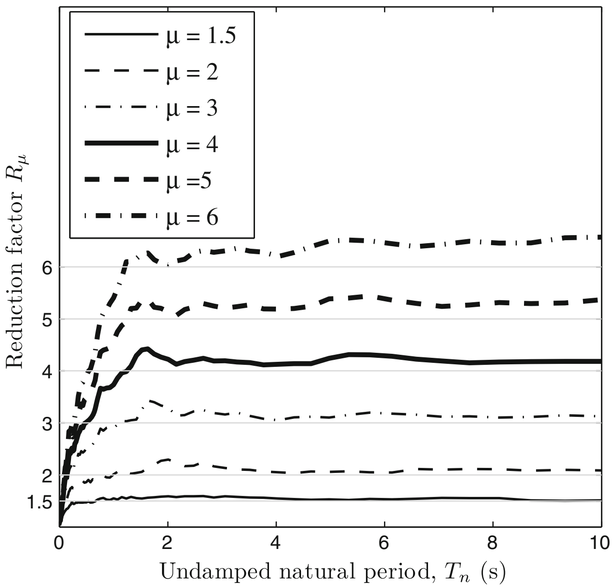

Fig. 20 Variation of force reduction factor with undamped natural period of SDOF and displacement ductility ratio

and the level of viscous damping was considered to be 5% for elastic as well as inelastic systems. Figure 20 displays the variation of mean force reduction factors with undamped natural periods of SDOF for six different values of target ductilities. It is observed that as $T_n \to 0$, $R_\mu \to 1$ The equal deformation rule of Veletsos and Newmark (1960) - at long periods, peak elastic deformation is equal to peak inelastic deformation, and therefore $R_\mu = \mu$- is apparently not strictly valid up to undamped natural periods of 10 s. Although the rule is conservative in the sense that it predicts lower values of R_μ, it is observed that the reduction factor at 10 s is about 10% higher than the assumed target displacement ductility. However, the results at long periods are likely to be influenced by the cut-off frequency of high-pass filters used in processing the accelerograms.

Following the pioneering works of Veletsos and Newmark (1960), several researchers have proposed mathematical equations describing the $R_\mu - \mu - T_n$ relationship (see, for example, Borzi and Elnashai 2000, and references therein). To establish such a relationship we use a mathematical model similar to the one used by Watanabe and Kawashima (2002). Their model was designed specifically to satisfy the equal deformation rule at long periods, which we calibrate to match the force reduction factors displayed in Fig. 20. We idealize mean force reduction factors by the following equations.

$$R_\mu = [\mu - 1]\,\psi\,(T_n) + 1 \tag{16}$$

$$\psi\,(T_n) = \frac{T_n - \gamma}{\gamma\,\exp\,(\tau T_n)} + 1 \tag{17}$$

In Eqs. 16 and 17, the constants γ, and τ are functions of μ and were accordingly calibrated using mean reduction factors presented in Fig. 20. The reduction factors given by these equations satisfy the condition $R_\mu \to 1$ as $T_n \to 0$. As $T_n \to \infty$, the force reduc-

Table 7 Parameters of Eqs. 16 and 17 describing the $R_\mu - \mu - T_n$ relationship

μ	γ	τ
1.5	0.50	6.00
2.0	1.00	4.50
3.0	2.00	3.00
4.0	2.50	2.00
5.0	3.00	1.75
6.0	3.25	1.50

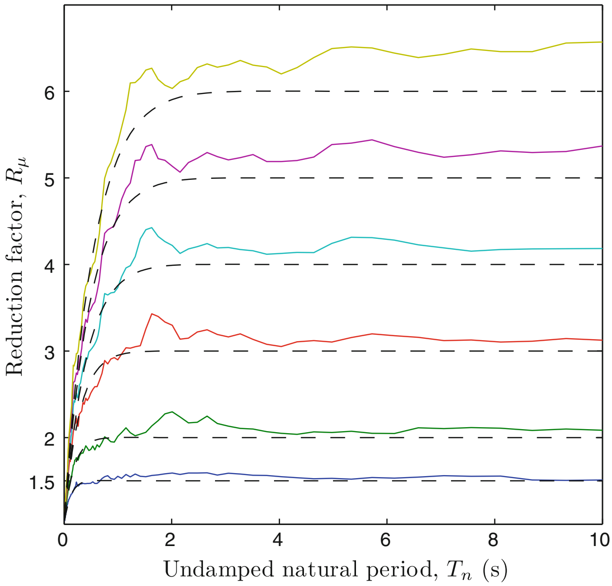

Fig. 21 Comparison of mean force reduction factors (*solid lines*) with the idealized ones (*dashed lines*) given by Eqs. 16 and 17 for displacement ductilities of 1.5, 2, 3, 4, 5, and 6

tion factor given by our equations approaches μ. The constants of Eqs. 16 and 17 are presented in Table 7. Figure 21 compares mean force reduction factors with the idealized ones. Note that the match between the average force reduction factors and the approximate ones given by Eqs. 16 and 17 show some differences at long periods. Considering the uncertainty in long-period response spectral ordinates, the calibration of the constants were judged based on structural periods up to about 4s. Even though force reduction factors are presented in Fig. 21 up to structural periods of 10 s, it should be noted that the model is constrained to follow the equal displacement rule at long periods.

It is important to note that force reduction factors of individual ground motion records show a considerable variation around the mean. In this sense it might not be conservative to use the mean force reduction factors. Ground motion prediction equations for inelastic spectral ordinates like the ones proposed by Rupakhety and Sigbjörnsson (2009a), and Bozorgnia et al. (2010) provide a more reliable estimate of design lateral strengths than the approach of using force reduction factors. The number of ground-motion records containing forward-directivity pulses is not sufficient to develop such a model.

Another important consideration to keep in mind while using force reduction factors is the level of damping in structures. Watanabe and Kawashima (2002) computed force reduction factors with three assumptions regarding the damping ratio of elastic and inelastic SDOF, namely (i) 2% for both elastic and inelastic systems, (ii) 5% for elastic and 2% for inelastic systems, and (iii) 5% for both elastic and inelastic systems. Their results indicated that the first assumption provides the largest force reduction factors, the second assumption provides the smallest force reduction factors, while the third one estimates force reduction factors between the two cases. We performed a similar study on our data, and the results were in agreement with their observations. Before applying force reduction factors, it is important to consider the assumptions regarding the damping ratio of SDOF used in deriving them. The reduction factors presented here correspond to 5% of critical damping for both elastic and inelastic SDOF systems.

9 Conclusions

A large number of recorded near-fault ground-motion data have been collected and studied, with special emphasis on forward-directivity effects. The period where 5% damped pseudo-spectral velocity contains a clear peak is proposed as a measure of predominant period (T_d) of forward-directivity affected near-fault ground motions. The main advantage of this definition is that, unlike pulse period as defined by various authors, this measure is unambiguous and is easily calculated. A robust equation is developed to relate T_d to earthquake magnitude. The relationship between T_d and M_w is similar to scaling relations between pulse period and magnitude proposed by different researchers in the past

An empirical model is developed to estimate peak ground velocity (*PGV*) as a function of earthquake magnitude and source-to-site distance. However, we found that the available data are not sufficient to constrain a reliable model for the effects of source mechanism and local site conditions. A weak dependence of *PGV* on moment magnitude is observed. A potentially useful predictor for directivity, based on the work of Spudich and Chiou (2008), is tested as a potential parameter in *PGV* attenuation model, although with limited success.

Properties of elastic response spectra of forward-directivity-affected near-fault ground motion are discussed in depth. A simple model is proposed to estimate mean spectral shapes of SDOF response to such ground motions. The proposed analytical model is a continuous function of the undamped natural period of SDOF oscillators, and its parameters are magnitude dependent. The model is calibrated by using recorded ground motions. The dependence of the parameters of the proposed model on earthquake size is investigated, constraining their relationship in a step-by-step manner. It was found that several parameters of the model can be effectively expressed in terms of earthquake size, thereby reducing the number of free variables.

In addition, the effects of viscous damping ratio on spectral shapes were thoroughly examined. By studying spectral shapes for different levels of viscous damping, we were able to express the parameters of the spectral shape model as a continuous function of damping ratio. This avoids the use of so-called damping correction factors commonly used to derive response spectra for various levels of damping from that corresponding to 5% of critical damping.

The proposed model is found to have small uncertainties in the period range of common engineering structures, whereas uncertainties concerned with very high frequencies are larger. The standard deviation of the residuals of the proposed model was found to be smaller for highly damped systems.. The proposed model can be used with any reliable attenuation model of *PGV*, in order to estimate the elastic response spectra for forward-directivity ground motion in the near-fault area.

Finally, constant-ductility spectra of elasto-plastic SDOF systems are studied for ductility ratios ranging from 1.5 to 6. An approximate equation to estimate force reduction factors as a function of displacement ductility and SDOF period is also presented.

Acknowledgments The first author acknowledges a grant from the research fund of the University of Iceland supporting his doctoral studies. The second author is financially supported by a research grant from Landsvirkjun's Energy Research Fund for his MSc project and his doctoral study is financially supported by RANNIS, the Icelandic Centre for Research, and the South Iceland University Center Dr. John Douglas read some parts of an earlier version of the manuscript and provided valuable comments. Professor Polat Gülkan provided several constructive comments on the manuscript. These comments are gratefully acknowledged. We also acknowledge insightful comments of an anonymous reviewer which resulted in significant improvements in the paper.

Appendix 1

Approximation of the response spectrum at long periods

To obtain an approximation we assume that the Fourier acceleration spectrum is proportional to ω when $\omega \to 0$, ω being the frequency. This assumption is in accordance with the Brune near-fault model (Brune 1970), according to which we have

$$|A_N(\omega)| \propto \omega \tag{A.1.1}$$

Hence, it follows that the velocity spectrum approaches a constant value for $\omega = 0$:

$$|V_N(0)| = \text{constant} \tag{A.1.2}$$

Using this basic property of the near-fault spectrum and random vibration theory, it is possible to derive the asymptote of the earthquake response spectrum when the natural structural period approaches infinity. The solution can be approximated as follows:

$$PSV \propto \frac{1}{\sqrt{T_n}} \left(\sqrt{2\log\left(\frac{2\Delta T}{T_n}\right)} + \frac{\gamma}{\sqrt{2\log\left(\frac{2\Delta T}{T_n}\right)}} \right) \sqrt{1 - \exp\left(-4\pi\zeta\frac{\Delta T}{T_n}\right)} \quad \text{if } T_n \gg T_d \tag{A.1.3}$$

where, T_n is the undamped natural period of the structure, ζ is the damping ratio, ΔT is the duration of strong-motion, T_d is the period of the spectral peak, and $\gamma = 0.5772$ is the Euler's constant.

We adopt the definition of Trifunac and Brady (1975) taking significant duration of the strong ground motion as the time interval between the 5% and the 95% of the Arias intensity (Arias 1970). Average duration for each magnitude bin listed in Table 3 in the text was computed accordingly. Using these duration values and 5% critical damping, Eq. A.1.3 was used to compute the asymptote of *PSV* at long periods. It should be noted that Eq. A.1.3 can not be used for $T_n \geq 2\Delta T$. In such cases, the second term in Eq. A.1.3 can be replaced by the peak factors given in Cartwright and Longuet-Higgins (1956).

Since the slope (in log-log scale) of the long period part of the proposed spectral shape model is controlled by θ, its value can be estimated to match the asymptote computed from Eq. A.1.3. The comparison between the proposed model and the asymptotic solution of Eq. A.1.3 for different magnitude bins is shown in Fig. 22 below. The asymptotic solution is hinged to the spectral shape at a period equal to two times the period of the spectral peak. The values of θ required to match the asymptotic slope was found to be lie between 1.9 for the first bin to 2.25 for the sixth bin. In order to simplify the model, we use a constant value of 2 for all magnitude bins. This is also consistent with the commonly used assumption that the PSV spectrum has a slope of -1 in a tripartite representation (see, for example, Newmark et al. 1973).

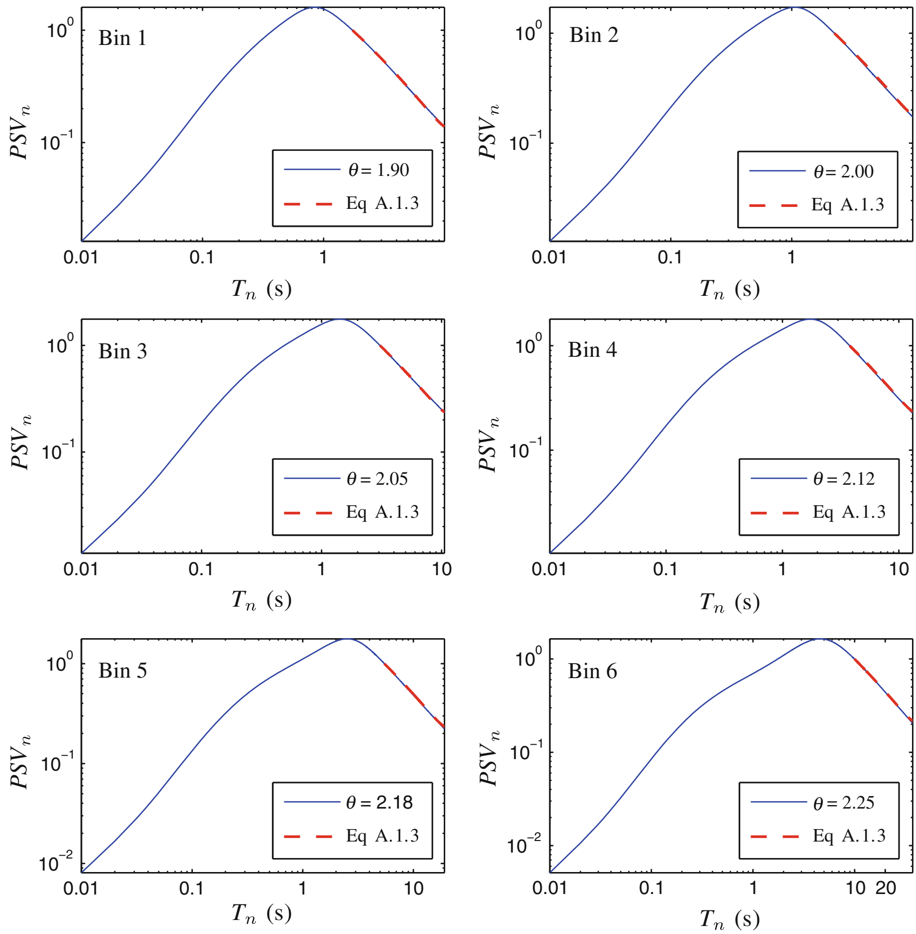

Fig. 22 Comparison between the asymptotic solution (red line) and the proposed spectral shapes (*blue line*) for different magnitude bins. The asymptotic solutions are hinged to the spectral shapes at a period two times the period of the spectral peak

Appendix 2

See Table 8.

Table 8 Near-fault records with distinct velocity pulses

EID	WID	Location	Date	Mechanism[1]	M_w	Station	Component[2]	PGV (cm/s)	Z[3] (km)	r_{epi}[4] (km)	r_{JB}[5] (km)	s[6] (km)	d[7] (km)	c[8]	$V_{s,30}$ (m/s)
1	1	Parkfield, CA, USA	27/06/1966	SS	6.19	CO2	SN	75.10	10.00	31.04	6.27	24.94	9.99	3.71	185
2	2	San Fernando, CA, USA	09/02/1971	RV	6.61	PCD	SN	116.50	13.00	11.86	0.00	4.02	21.87	1.85	2016
3	3	Tabas, Iran	16/09/1978	RV	7.11	TAB	SP	121.87	5.75	55.24	1.79	53.92	11.27	3.59	767
4	4	Coyote lake, CA, USA	08/06/1979	SS	5.74	GA6	SN	51.50	9.60	4.37	0.42	4.10	5.00	3.12	663
5	5	Imperial Valley, CA, USA	15/10/1979	SS	6.53	Aeroporto Mexicalli	SN	44.30	9.96	2.47	0.00	2.03	10.05	3.54	275
5	6	Imperial Valley, CA, USA	15/10/1979	SS	6.53	Agrarias	SN	54.40	9.96	2.62	0.00	2.38	10.00	3.22	275
5	7	Imperial Valley, CA, USA	15/10/1979	SS	6.53	Brawley airport	SN	36.12	9.96	43.15	8.54	38.13	8.44	2.61	209
5	8	Imperial Valley, CA, USA	15/10/1979	SS	6.53	EC county center FF	SN	54.50	9.96	29.07	7.31	27.62	10.11	2.20	192
5	9	Imperial Valley, CA, USA	15/10/1979	SS	6.53	EC Meloland Overpass FF	SN	115.04	9.96	19.44	0.07	19.35	10.11	3.95	186
5	10	Imperial Valley, CA, USA	15/10/1979	SS	6.53	E10	SN	46.92	9.96	26.31	6.17	25.09	10.11	2.28	203
5	11	Imperial Valley, CA, USA	15/10/1979	SS	6.53	E03	SN	41.10	9.96	28.65	10.79	26.32	7.85	1.63	163
5	12	Imperial Valley, CA, USA	15/10/1979	SS	6.53	E04	SN	77.93	9.96	27.13	4.90	26.59	8.87	2.13	209
5	13	Imperial Valley, CA, USA	15/10/1979	SS	6.53	E05	SN	91.48	9.96	27.80	1.76	27.71	9.42	2.66	206
5	14	Imperial Valley, CA, USA	15/10/1979	SS	6.53	E06	SN	111.87	9.96	27.47	0.00	27.47	9.87	3.39	203

Table 8 Continued

EID	WID	Location	Date	Mechanism[1]	M_w	Station	Component[2]	PGV (cm/s)	Z^3 (km)	r_{epi}[4] (km)	r_{JB}[5] (km)	s[6] (km)	d[7] (km)	c[8]	$V_{s,30}$ (m/s)
5	15	Imperial Valley, CA, USA	15/10/1979	SS	6.53	E07	SN	108.82	9.96	27.64	0.56	27.54	10.11	3.73	211
5	16	Imperial Valley, CA, USA	15/10/1979	SS	6.53	E08	SN	48.55	9.96	28.09	3.86	27.52	10.11	2.74	206
5	17	Imperial Valley, CA, USA	15/10/1979	SS	6.53	El Centro Differential Array	SN	59.61	9.96	27.23	5.09	26.36	10.11	2.48	202
5	18	Imperial Valley, CA, USA	15/10/1979	SS	6.53	Holtville Post Office	SN	55.15	9.96	19.81	5.51	18.87	8.76	1.81	203
6	19	Mexicalli Valley, Mexico	09/06/1980	SS	6.33	VCT	SN	76.71	11.00	11.79	6.07	10.11	7.00	1.89	275
7	20	Irpinia, Italy-01	23/11/1980	NM	6.9	Sturno	SN	41.50	9.50	30.35	6.78	24.14	5.68	2.47	1000
8	21	Westmorland	26/04/1981	SS	5.9	Parachute test site	SN	35.85	2.30	20.47	16.54	5.99	0.30	1.68	349
9	22	Morgan Hill, CA, USA	24/04/1984	SS	6.19	Gilroy Array # 6	SN	35.39	8.50	36.34	9.85	26.51	8.00	3.87	663
9	23	Morgan Hill, CA, USA	24/04/1984	SS	6.19	HAL	SN	39.55	8.50	3.94	3.45	0.49	8.00	1.94	282
10	24	Palm Springs, CA, USA	08/07/1986	OB	6.06	NPS	SN	73.63	11.00	10.57	0.00	8.54	9.75	2.60	345
10	25	Palm Springs, CA, USA	08/07/1986	OB	6.06	DSP	SN	29.69	11.00	10.38	0.99	9.31	8.79	1.66	345
11	26	San Salvador	10/10/1986	SS	5.8	Geotech Investigation center	SN	62.26	10.90	7.93	2.14	6.00	5.00	3.03	545
12	27	Whittier Narrows, CA, USA	10/10/1987	OB	5.99	DOW	SN	30.40	14.60	16.04	14.95	4.99	0.19	0.93	272
12	28	Whittier Narrows, CA, USA	10/10/1987	OB	5.99	LB Orange Eve	SN	32.88	14.60	20.68	19.80	4.99	0.19	0.91	270
13	29	Superstition Hills, CA, USA	24/11/1987	SS	6.54	PTS	SN	106.76	9.00	15.99	0.95	15.96	9.00	3.33	349
13	30	Superstition Hills, CA, USA	24/11/1987	SS	6.54	ELC	SN	52.05	9.00	35.83	18.20	18.00	9.00	3.14	192
14	31	Loma Prieta, CA, USA	17/10/1989	OB	6.93	Alameda Naval Air Stn Hanger	SN	32.16	17.48	90.77	70.90	20.02	14.53	2.61	190
14	32	Loma Prieta, CA, USA	17/10/1989	OB	6.93	Gilroy Array #2	SN	45.67	17.48	29.77	10.38	19.98	14.53	3.33	271
14	33	Loma Prieta, CA, USA	17/10/1989	OB	6.93	Oakland Outer Harbor Wharf	SN	49.21	17.48	94.00	74.16	20.02	14.53	2.59	249
14	34	Loma Prieta, CA, USA	17/10/1989	OB	6.93	LGP	SN	101.68	17.48	18.46	0.00	17.88	14.53	3.18	478

Table 8 Continued

EID	WID	Location	Date	Mechanism[1]	M_w	Station	Component[2]	PGV (cm/s)	Z^3 (km)	r_{epi}[4] (km)	r_{JB}[5] (km)	s[6] (km)	d[7] (km)	c[8]	$V_{s,30}$ (m/s)
14	35	Loma Prieta, CA, USA	17/10/1989	OB	6.93	STG	SN	57.23	17.48	27.23	7.58	20.02	14.53	3.50	371
15	36	Sierra Madre, CA, USA	28/06/1991	RV	5.56	COG	Rad (filt)	14.99	NA	NA	NA	NA	NA	NA	NA
16	37	Erzincan, Turkey	13/03/1992	SS	6.69	ERZ	SN	95.42	9.00	8.97	0.00	8.97	6.00	2.09	275
17	38	Cape Mendocino	25/04/1992	RV	7	Petrolia	SN	82.10	9.60	4.51	0.00	0.49	6.65	1.11	713
18	39	Landers, CA, USA	28/06/1992	SS	7.28	LUC	SN	123.11	7.00	44.02	2.19	47.54	6.99	2.72	685
18	40	Landers, CA, USA	28/06/1992	SS	7.28	Yermo Fire Station	SN	53.22	7.00	85.99	23.62	65.81	6.99	3.30	354
19	41	Northridge, CA, USA	17/01/1994	RV	6.7	JFA	SN	67.43	17.50	12.97	0.00	1.76	19.50	2.41	373
19	42	Northridge, CA, USA	17/01/1994	RV	6.7	JFA generator	SN	67.38	17.50	13.00	0.00	1.97	19.50	2.41	526
19	43	Northridge, CA, USA	17/01/1994	RV	6.7	LA Wadsworth VA hospital North	SN	32.38	17.50	19.55	14.55	3.88	3.99	1.29	392
19	44	Northridge, CA, USA	17/01/1994	RV	6.7	LA Dam (LDW)	SN	77.11	17.50	11.79	0.00	0.33	19.50	2.12	629
19	45	Northridge, CA, USA	17/01/1994	RV	6.7	NWS	SN	87.75	17.50	21.55	2.11	14.13	19.50	3.08	286
19	46	Northridge, CA, USA	17/01/1994	RV	6.7	Pacoima dam (upper left)	SN	107.08	17.50	20.36	4.92	3.88	19.50	3.97	2016
19	47	Northridge, CA, USA	17/01/1994	RV	6.7	RRS	SN	167.20	17.50	10.91	0.00	1.48	19.50	1.89	282
19	48	Northridge, CA, USA	17/01/1994	RV	6.7	SCG	SN	130.27	17.50	13.11	0.00	1.23	19.50	2.47	251
19	49	Northridge, CA, USA	17/01/1994	RV	6.7	SCH	SN	116.56	17.50	13.60	0.00	0.59	19.50	2.63	371
19	50	Northridge, CA, USA	17/01/1994	RV	6.7	Sylmar Olive View Medical FF	SN	122.73	17.50	16.77	1.74	1.47	19.50	3.56	441
20	51	Kobe, Japan	19/01/1995	RV	6.9	Takarazuka	SN	72.65	17.90	38.60	0.00	38.61	17.41	3.97	312
21	52	Izmit, Tukey	17/08/1999	SS	7.51	ARC	SN	29.38	15.00	53.68	10.56	47.42	13.06	2.60	523
21	53	Izmit, Tukey	17/08/1999	SS	7.51	GBZ	SN	45.68	15.00	47.03	7.57	46.58	13.09	2.23	792
22	54	Chi-Chi, Taiwan	20/09/1999	OB	7.6	CHY006	SN	64.72	6.76	40.47	9.77	35.04	9.13	3.22	438

Table 8 Continued

EID	WID	Location	Date	Mechanism[1]	M_w	Station	Component[2]	PGV (cm/s)	Z^3 (km)	$r_{epi}{}^4$ (km)	$r_{JB}{}^5$ (km)	s^6 (km)	d^7 (km)	c^8	$V_{s,30}$ (m/s)
22	55	Chi-Chi, Taiwan	20/09/1999	OB	7.6	TCU031	SN	59.86	6.76	80.09	30.18	49.95	14.88	2.57	489
22	56	Chi-Chi, Taiwan	20/09/1999	OB	7.6	TCU036	SN	62.43	6.76	67.81	19.84	49.95	14.88	3.43	273
22	57	Chi-Chi, Taiwan	20/09/1999	OB	7.6	TCU038	SN	50.86	6.76	73.11	25.44	49.95	14.88	3.36	273
22	58	Chi-Chi, Taiwan	20/09/1999	OB	7.6	TCU040	SN	53.00	6.76	69.04	22.08	49.95	14.88	3.21	362
22	59	Chi-Chi, Taiwan	20/09/1999	OB	7.6	TCU042	SN	47.34	6.76	78.37	26.32	49.95	14.88	2.84	273
22	60	Chi-Chi, Taiwan	20/09/1999	OB	7.6	TCU046	SN	43.96	6.76	68.89	16.74	49.95	14.75	2.86	466
22	61	Chi-Chi, Taiwan	20/09/1999	OB	7.6	TCU049	SN	44.82	6.76	38.91	3.78	35.94	14.88	2.87	487
22	62	Chi-Chi, Taiwan	20/09/1999	OB	7.6	TCU053	SN	41.90	6.76	41.20	5.97	35.39	14.88	2.64	455
22	63	Chi-Chi, Taiwan	20/09/1999	OB	7.6	TCU054	SN	60.92	6.76	37.64	5.30	31.67	14.88	2.65	461
22	64	Chi-Chi, Taiwan	20/09/1999	OB	7.6	TCU065	SN	127.68	6.76	26.67	0.59	20.30	14.19	3.79	306
22	65	Chi-Chi, Taiwan	20/09/1999	OB	7.6	TCU075	SN	88.44	6.76	20.67	0.91	13.20	13.39	3.71	573
22	66	Chi-Chi, Taiwan	20/09/1999	OB	7.6	TCU076	SN	63.73	6.76	16.03	2.76	5.42	11.75	3.50	615
22	67	Chi-Chi, Taiwan	20/09/1999	OB	7.6	TCU082	SN	56.12	6.76	36.20	5.18	30.15	14.88	2.65	473
22	68	Chi-Chi, Taiwan	20/09/1999	OB	7.6	TCU103	SN	62.18	6.76	52.43	6.10	43.39	14.88	3.11	494
22	69	Chi-Chi, Taiwan	20/09/1999	OB	7.6	TCU128	SN	78.66	6.76	63.29	13.15	49.95	14.88	2.61	600
22	70	Chi-Chi, Taiwan	20/09/1999	OB	7.6	TCU129	SN	70.08	6.76	14.16	1.84	4.34	10.53	3.70	664
23	73	Chi-Chi, Taiwan aftershock	20/09/1999	RV	6.2	TCU076	SN	33.10	8.00	20.80	13.04	4.50	6.46	3.46	615
23	71	Chi-Chi, Taiwan aftershock	20/09/1999	RV	6.2	CHY024	SN	69.93	8.00	25.52	18.47	5.51	6.46	2.37	428
23	72	Chi-Chi, Taiwan aftershock	20/09/1999	RV	6.2	CHY080	SN	59.35	8.00	29.48	21.34	5.51	6.46	3.41	553
24	74	Chi-Chi, Taiwan aftershock	25/09/1999	RV	6.3	CHY101	SN	36.26	16.00	49.98	34.55	14.99	12.01	2.56	259

Table 8 Continued

EID	WID	Location	Date	Mechanism[1]	M_w	Station	Component[2]	PGV (cm/s)	Z^3 (km)	r_{epi}[4] (km)	r_{JB}[5] (km)	s^6 (km)	d^7 (km)	c^8	$V_{s,30}$ (m/s)
25	75	South Iceland	17/06/2000	SS	6.57	Flagbjarnarholt	SN	73.84	6.00	5.29	4.20	1.85	6.00	1.32	800
26	76	South Iceland	21/06/2000	SS	6.49	Thorsarbru	SN	82.02	5.00	5.32	2.80	6.17	5.00	1.28	800
26	77	South Iceland	21/06/2000	SS	6.49	Thorsartun	SN	67.14	5.00	5.59	3.60	6.17	5.00	1.49	800
26	78	South Iceland	21/06/2000	SS	6.49	Solheimar	SN	109.99	5.00	11.02	4.10	9.88	5.00	1.75	560
27	79	Parkfield, CA, USA	28/09/2004	SS	6	Parkfield fault zone 12	SN	57.50	8.10	11.08	0.94	23.44	8.10	1.36	339
27	80	Parkfield, CA, USA	28/09/2004	SS	6	Parkfield Cholame 2 west	SN	49.98	8.10	11.53	1.88	10.00	8.10	3.32	185
27	81	Parkfield, CA, USA	28/09/2004	SS	6	Parkfield Cholame 2 east	SN	23.67	8.10	11.63	2.50	10.00	8.10	2.92	376
27	82	Parkfield, CA, USA	28/09/2004	SS	6	Parkfield fault zone 1	SN	64.15	8.10	8.39	0.00	8.44	8.10	3.95	339
27	83	Parkfield, CA, USA	28/09/2004	SS	6	Parkfield Cholame 3 west	SN	45.00	8.10	11.88	2.50	10.00	8.10	3.06	339
27	84	Parkfield, CA, USA	28/09/2004	SS	6	Parkfield Cholame 4 west	SN	38.37	8.10	12.37	3.44	10.00	8.10	2.71	438
27	85	Parkfield, CA, USA	28/09/2004	SS	6	Parkfield Cholame 4A west	SN	22.16	8.10	13.01	4.69	10.00	8.10	2.36	339
27	86	Parkfield, CA, USA	28/09/2004	SS	6	Parkfield Stone Corral 1 east	SN	44.95	8.10	7.17	2.81	6.25	8.10	2.14	339

Table 8 Continued

27	87	Parkfield, CA, USA	28/09/2004	SS	6	Parkfield fault zone 9	SN	26.10	8.10	9.98	1.25	10.00	8.10	2.87	438
27	88	Parkfield, CA, USA	28/09/2004	SS	6	Parkfield Cholame 3 east	SN	34.54	8.10	11.86	5.63	10.00	8.10	1.75	376
27	89	Parkfield, CA, USA	28/09/2004	SS	6	Parkfield Cholame 1 east	SN	53.10	8.10	11.56	1.88	10.00	8.10	3.34	339
28	90	Ölfus, South Iceland	25/05/2008	SS	6.3	EERC, Basement	SN	41.13	5.00	8.00	3.33	4.94	5.00	1.27	800
28	91	Ölfus, South Iceland	25/05/2008	SS	6.3	Selfoss City Hall	SN	33.03	5.00	8.00	3.33	4.94	5.00	1.27	800
28	92	Ölfus, South Iceland	25/05/2008	SS	6.3	Hveragerdi Retirement House	SN	54.31	5.00	3.00	1.40	4.94	5.00	1.30	800
29	93	L'Aquila, Italy	06/04/2009	NM	6.3	AQK	SN	46.57	NA	4.00	0.00	NA	NA	NA	580

[1] SS, strike-slip; RV, reverse; OB, oblique; NM, normal
[2] SN, strike-normal; SP, strike-parallel
[3] Hypocentral depth
[4] Epicentral distance
[5] Joyner and Boore distance
[6] Length of fault that ruptures towards site
[7] Width of fault that ruptures towards site
[8] Isochrone velocity normalized by the shear wave velocity (Spudich et al. 2004)

References

Abrahamson NA (2000) Effects of rupture directivity on probabilistic seismic hazard analysis. In: Proceedings of the 6th international conference on seismic zonation: managing earthquake risk in the 21st century, Earthquake Engineering Research Institute, University of California, Berkeley

Abrahamson NA, Silva WJ (1997) Empirical response spectral attenuation relations for shallow crustal earthquakes. Seismol Res Lett 68(1):94–127

Abrahamson NA, Atkinson G, Bozorgnia Y, Campbell K, Chiou B, Idriss IM, Silva W, Youngs R (2008) Comparisons of the NGA ground-motion relations. Earthq Spectr 24(1):45–66

Akkar S, Bommer JJ (2007) Prediction of elastic displacement response spectra in Europe and the Middle East. Earthq Eng Struct Dyn 36(10):1275–1301

Alavi B, Krawinkler H (2000) Effects of near-fault ground motions on frame structures. Technical report 138, John A Blume Earthquake Engineering Center, Stanford University, Stanford, California

Alavi B, Krawinkler H (2004) Behavior of moment-resisting frame structures subjected to near-fault ground motions. Earthq Eng Struct Dyn 33(6):687–706

Ambraseys N, Smit P, Douglas J, Margaris B, Sigbjörnsson R, Ólafsson S, Suhadolc P, Costa G (2004) Internet site for European strong-motion data. Bollettino di Geofisica Teorica ed Applicata 45(3):113–129

Ambraseys NN, Douglas J, Sarma SK, Smit PM (2005) Equations for the estimation of strong ground motions from shallow crustal earthquakes using data from Europe and the Middle East: horizontal peak ground acceleration and spectral acceleration. Bull Earthq Eng 3(1):1–53

Anderson JC, Bertero VV, Bertero RD (1999) Performance improvement of long period building structures subjected to severe pulse-type ground motions. Technical report PEER-1999/09, Pacific Earthquake Engineering Research Center, University of California, Berkeley

Arias A (1970) A measure of earthquake intensity. In: Hansen RJ (ed) Seismic design for nuclear power plants, vol 23. MIT Press, Cambridge, Massachusetts, pp 438–483

Baker JW (2007) Quantitative classification of near-fault ground motions using wavelet analysis. Bull Seismol Soc Am 97(5):1486–1501

Biot M (1933) Theory of elastic systems vibrating under transient impulse with an application to earthquake-proof buildings. Proc Natl Acad Sci USA 19(2):262–268

Bommer JJ, Alarcon JE (2006) The prediction and use of peak ground velocity. J Earthq Eng 10(1):1–31

Boore DM, Joyner WB, Fumal TE (1997) Equations for estimating horizontal response spectra and peak acceleration from western north American earthquakes: a summary of recent work. Seismol Res Lett 68(1):128–153

Borzi B, Elnashai AS (2000) Refined force reduction factors for seismic design. Eng Struct 22(10):1244–1260

Bozorgnia Y, Hachem MM, Campbell KW (2010) Ground motion prediction equation ("attenuation relationship") for inelastic response spectra. Earthq Spectr 26:1–23

Bray JD, Rodriguez-Marek A (2004) Characterization of forward-directivity ground motions in the near-fault region. Soil Dyn Earthq Eng 24(11):815–828

Brune J (1970) Tectonic stress and the spectra of shear waves from earthquakes. J Geophy Res 75:4997–5009

Cartwright DE, Longuet-Higgins MS (1956) The statistical distribution of the Maxima of a random function. Proceedings of the Royal Society of London. Math Phys Sci 237(1209):212–232

CEN (2004) EN 1998-1 Eurocode 8: design of structures for earthquake resistance, part 1: general rules, seismic actions and rules for buildings. European committee for Standardization

Douglas J (2003) Earthquake ground motion estimation using strong-motion records: a review of equations for the estimation of peak ground acceleration and response spectral ordinates. Earth Sci Rev 61(1–2):43–104

Dreger DS, Gee L, Lombard P, Murray MH, Romanowicz B (2005) Rapid finite-source analysis and near-fault strong ground motions: application to the 2003 mw 6.5 San Simeon and 2004 Mw 6.0 Parkfield earthquakes. Seismol Res Lett 76(1):40–48

Graizer V, Kalkan E (2009) Prediction of spectral acceleration response ordinates based on PGA attenuation. Earthq Spectr 25:39–69

Halldórsson B, Ólafsson S, Sigbjörnsson R (2007) A fast and efficient simulation of the Far-Fault and Near-Fault earthquake ground motions associated with the June 17 and 21, 2000, earthquakes in South Iceland. J Earthq Eng 11:343–370

Halldorsson B, Mavroeidis GP, Papageorgiou AS (2010) Near-fault and far-field strong ground motion simulation for earthquake engineering applications using the specific barrier model. ASCE J Struct Eng (accepted, in press)

Heaton TH, Hall JF, Wald DJ, Halling MW (1995) Response of high-rise and base-isolated buildings to a hypothetical mw 7.0 blind thrust earthquake. Science 267(5195):206–211

Housner GW (1959) Behavior of structures during earthquakes. J Eng Mech Div 85(14):109–129

Jalali RS, Trifunac MD (2008) A note on strength-reduction factors for design of structures near earthquake faults. Soil Dyn Earthq Eng 28(3):212–222

Joyner WB, Boore DM (1993) Methods for regression analysis of strong-motion data. Bull Seismol Soc Am 83(2):469–487

Kim A, Dreger DS (2008) Rupture process of the 2004 Parkfield earthquake from near-fault seismic waveform and geodetic records. J Geophys Res Solid Earth 113(B7):B07, 308

Langbein J, Borcherdt R, Dreger D, Fletcher J, Hardebeck JL, Hellweg M, Ji C, Johnston M, Murray JR, Nadeau R, Rymer MJ, Treiman JA (2005) Preliminary report on the 28 September 2004, m 6.0 Parkfield, California earthquake. Seismol Res Lett 76(1):10–26

Lin YY, Chang KC (2003) Study on damping reduction factor for buildings under earthquake ground motions. J Struct Eng 129(2):206–214

Liu P, Custodio S, Archuleta RJ (2006) Kinematic inversion of the 2004 m 6.0 Parkfield earthquake including an approximation to site effects. Bull Seismol Soc Am 96(4B):S143–S158

Luzi L, Hailemikael S, Bindi D, Pacor F, Mele F, Sabetta F (2008) ITACA (ITalian accelerometric archive): a web portal for the dissemination of Italian strong-motion data. Seismol Res Lett 79(5):716–722

Makris N (1997) Rigidity-plasticity-viscosity: can electrorheological dampers protect base isolated structures from near-source ground motions?. Earthq Eng Struct Dyn 26(5):571–592

Mavroeidis GP, Papageorgiou AS (2003) A mathematical representation of near-fault ground motions. Bull Seismol Soc Am 93(3):1099–1131

Mavroeidis GP, Dong G, Papageorgiou AS (2004) Near-fault ground motions, and the response of elastic and inelastic single-degree-of-freedom (SDOF) systems. Earthq Eng Struct Dyn 33(9):1023–1050

Miranda E, Bertero VV (1994) Evaluation of strength reduction factors for earthquake resistant design. Earthq Spectr 10(2):357–379

Newmark NM, Blume JA, Kapur KK (1973) Seismic design spectra for nuclear power plants. J Power Div 99(2):287–303

Power M, Chiou B, Abrahamson N, Roblee C (2006) The next generation of ground motion attenuation models (NGA) project: an overview. In: Proceedings of the 8th national conference on earthquake engineering, pp 18–21

Rupakhety R, Sigbjörnsson R (2009) Ground-motion prediction equations (GMPEs) for inelastic response and structural behaviour factors. Bull Earthq Eng 7(3):637–659

Rupakhety R, Sigbjörnsson R (2009) Ground-motion prediction equations (GMPEs) for inelastic displacement and ductility demands of constant-strength SDOF systems. Bull Earthq Eng 7(3):661–679

Rupakhety R, Halldórsson B, Sigbjörnsson R (2010) Estimating coseismic deformations from near source strong motion records: methods and case studies. Bull Earthq Eng 8(4):787–811

Sadigh K, Chang CY, Egan JA, Makdisi F, Youngs RR (1997) Attenuation relationships for shallow crustal earthquakes based on California strong motion data. Seismol Res Lett 68(1):180–189

Shakal A, Graizer V, Huang M, Borcherdt R, Haddadi H, Lin K, Stephens C, Roffers P (2005) Preliminary analysis of strong-motion recordings from the 28 September 2004 Parkfield, California earthquake. Seismol Res Lett 76(1):27–39

Sigbjörnsson R, Ólafsson S (2004) On the South Iceland earthquakes in June 2000: strong motion effects and damage. Bollettino di Geofisica teorica ed applicata 45(3):131–152

Sigbjörnsson R, Snæbjörnsson JT, Higgins SM, Halldorsson B, Ólafsson S (2009) A note on the Mw 6.3 earthquake in Iceland on 29 May 2008 at 15: 45 UTC. Bull Earthq Eng 7(1):113–126

Somerville P (1998) Development of an improved representation of near-fault ground motions. SMIP98-CDMG, Oakland, California, pp 1–20

Somerville PG, Smith NF, Graves RW, Abrahamson NA (1997) Modification of empirical strong motion attenuation relations to include the amplitude and duration effects of rupture directivity. Seismol Res Lett 68(1):199–222

Somerville P, Irikura K, Graves R, Sawada S, Wald D, Abrahamson N, Iwasaki Y, Kagawa T, Smith N, Kowada A (1999) Characterizing crustal earthquake slip models for the prediction of strong ground motion. Seismol Res Lett 70(1):59–80

Somerville PG (2000) Magnitude scaling of near fault ground motions. In: Proceedings of international workshop on annual commemoration of Chi-Chi earthquake, pp 18–20

Spudich P, Chiou BS (2008) Directivity in NGA earthquake ground motions: analysis using isochrone theory. Earthq Spectr 24(1):279–298

Spudich P, Chiou BS, Graves R, Collins N, Somerville P (2004) A formulation of directivity for earthquake sources using isochrone theory. Technical report 2004–1268, US Geological Survey. Open-File Report

Tothong P, Cornell CA, Baker JW (2007) Explicit directivity-pulse inclusion in probabilistic seismic hazard analysis. Earthq Spectr 23(4):867–891

Trifunac MD, Brady AG (1975) A study on the duration of strong earthquake ground motion. Bull Seismol Soc Am 65:584–626

Veletsos AS, Newmark NM (1960) Effect of inelastic behaviour on the response of simple systems to earthquake motions. In: Proceedings of the 2nd world conference on earthquake engineering, vol 2, pp 895–912

Watanabe G, Kawashima K (2002) An evaluation of the force reduction factor in the force based seismic design. NIST special publication SP, pp 201–218